The Precision Measurement of the Neutron Lifetime Using Magnetically Trapped Neutrons: Marginally Trapped Neutrons and Fluorescent Time Constants

by

Carlo Egon Heinrich Mattoni

Submitted to the Department of Physics
in partial fulfillment of the requirements for the degree of

Bachelor of Arts

at

HARVARD UNIVERSITY

June 1995

Author .....
Department of Physics
May 1, 1995

Certified by .....
John M. Doyle
Assistant Professor of Physics
Thesis Supervisor

Accepted by .....
Gary Feldman
Chairman, Department of Physics

The Precision Measurement of the Neutron Lifetime Using Magnetically Trapped Neutrons: Marginally Trapped Neutrons and Fluorescent Time Constants

by

Carlo Egon Heinrich Mattoni

Submitted to the Department of Physics
on May 1, 1995, in partial fulfillment of the
requirements for the degree of
Bachelor of Arts

Abstract

A new magnetic trap-based method of measuring the lifetime (τ_β) of the free neutron has recently been proposed [1]. The success of the proposed method depends on assuring that the only significant neutron loss from the trap is beta decay. One potential spurious loss mechanism is the delayed escape of those neutrons with energy higher than the trap depth. Computer simulations of neutron trajectories in two proposed trap configurations, linear quadrupole and "multi-helmholtz," were performed. Results suggest that escape times for particles with energy higher than the trap depth are exponentially distributed. Over one percent of neutrons with energy 119-120% of the trap depth escape between 10 and 100 seconds after they are trapped. In order to achieve the accuracy of $10^{-5}\tau_\beta$, this systematic error will need to be eliminated or carefully characterized.

The proposed method for detecting the trapped neutron decays relies on fluorescent materials for down-converting the UV scintillations generated by the beta-decay electrons passing through liquid helium. The fluorescent decay behavior of ultraviolet down-converting phosphors was experimentally measured. The time response of the fluorescence of several possible materials, tetraphenyl-butadiene, sodium salicylate, and diphenylstilbene was studied. Using a chopped 243 nm coherent light beam, the decay time of fluorescence of these three compounds was measured at room temperature and at liquid-helium temperatures. Time constants of 2.3 ms and 9.0 ms were determined for TPB and NaSal, respectively, at 4K. The combination of TPB having the shortest measured time constant and a previously-measured 200% quantum efficiency makes it the most promising candidate for further exploration.

Thesis Supervisor: John M. Doyle
Title: Assistant Professor of Physics

Acknowledgments

My thanks first and foremost is to my parents. The debt of gratitude that I owe you for many years of unfailing support, both emotional and financial, is incalculable. Moreover, I am most grateful that you taught me the love of learning and instilled in me a desire to push myself to my own limits.

My thanks also is to my friends, especially Koji Takasumi, Venk Reddy, Joe Domilici, and Dean Tantillo. My friendship with the four of you has enriched my college experience throughout.

I especially thank Adam Polcyn for his collaborative effort on the measuments of fluorescent decay constants. Not only did I learn a great deal about the practical techniques of experimental physics by working with you, but I appreciated your ability to make our collaboration frictionless. My thanks also to the entire MIT spin-polarized hydrogen group, particularly Professor Thomas Greytak, for providing the equipment and lab space for the fluorescent materials measurements.

Finally, I would like to thank my advisor, John Doyle, for his guidance throughout the time leading up to and during the preparation of this thesis. My experience in your group has rekindled and focused my excitement about physics and taught me more than I ever wanted to know. I only hope that the coming years will be as pleasant and productive as the past year and a half.

Contents

List of Figures

List of Tables

Chapter 1

Precision Measurement of the Neutron Lifetime

1.1 General Introduction

The neutron beta-decay lifetime (τ_β) is a fundamental physical quantity whose value, in combination with other experimental data, can be used to perform internal consistency checks on the Standard Model. Such tests include searches for right-handed currents and tests of the unitarity of the Cabbibo-Kobayashi-Maskawa mixing matrix. Using the Standard Model, the neutron lifetime in combination with the A correlation coefficient in neutron decay can be used to extract the weak force coupling constants g_a and g_v. A check on the consistency of the standard model can be performed by comparing the value g_v thus obtained to that extracted from $0^+ - 0^-$ beta decays. Furthermore, the neutron lifetime provides an essential parameter for the model of Big Bang Nucleosynthesis, and can be used to check the consistency of that model as well as improve the accuracy of its predictions regarding the limits on the universal baryon density and the nature of cosmic "dark matter." [2][3][4]

The current accepted value of τ_β is based upon four recent experiments, each reporting errors less than 1%. The mean value of the measurements is 887.4 s with a 1σ confidence interval of 1.7 s [2]. Several experiments in progress aim to improve this measurement, but none of them are expected to provide an error smaller than a

Figure 1-1: Outline of the proposed experimental apparatus. From Doyle [5, Figure 1].

factor of 3 below that of the current measurements.

1.2 Proposed Method

A new approach to the precise measurement of τ_β has been proposed by Doyle and Lamoreaux [1][5]. This method relies on the production and storage of ultra-cold neutrons (UCN) in a magnetic trap filled with superfluid ^{4}He. Figure 1-1 shows the proposed experimental apparatus.

Magnetic trapping of neutrons occurs due to the interaction of the magnetic moment of the neutron (0.7 mK/T) with a magnetic field gradient. By creating a field minimum, neutrons in the low-field-seeking spin-state can be localized in the trapping region. Two proposed trapping configurations are discussed below, but both share the characteristic that they are roughly cylindrical in shape with the long axis parallel to the neutron beam axis. Since such a magnetic potential is conservative, in order to trap the neutrons it is necessary to dissipate the energy of neutrons while they are in the trapping region.

Dissipation of neutron energy (and therefore production of UCN) in the trapping region can take place by inelastic scattering of 8.9 Å neutrons off of superfluid ^{4}He using the "superthermal" process [6, page 461]. The superthermal technique is based on the phenomenon that the free neutron dispersion curve and the Landau-Feynman dispersion curve for single phonon emission cross only at zero energy and 11K (which corresponds to a neutron wavelength of 8.9 Å). Hence only neutrons with kinetic energies of 11K can interact with phonons. While the downscattering of incident 11K neutrons to near-rest is energetically favorable, the inverse process is suppressed by the Boltzman factor of $e^{-11K/T}$ where $T < 1$K is the temperature of the superfluid bath. At temperatures less than 1K, the dominant mechanism for upscattering is a two-phonon process, with a temperature dependence of

$$\tau_{2-phonon} \approx 10^2/T^7.$$

Thus neutron upscattering lifetimes on the order of $10^5\tau_\beta$ should be attainable by maintaining the temperature of the superfluid ^{4}He bath below 150 mK [1].

Also important to the improved measurement of τ_β is a new method for detecting beta-decays. When the neutrons beta-decay, the passage of energetic charged particles through the helium results in ultraviolet scintillations. Detection of neutron decays occurs by photodetection of the light produced by the helium scintillation. The high-energy electrons produced in the beta decay cause the superfluid helium to emit photons in the 50-100 nm range [7]. The inner wall of the cell may be constructed from polycarbonate coated with a phosphor-doped acrylic suitable for converting the UV light produced in the helium scintillations into visible light. The visible light may then be piped by the cell itself (by coating the exterior with a silver reflective film) to the exterior of the experimental apparatus.

1.3 Relationship of the current work to neutron lifetime measurement

The proposal discussed above purports to provide a method to measure τ_β with a systematic error at or below one part in 10^5 (using the cold beam source at ILL) [5]. The attainable precision in the neutron lifetime measurement is claimed to be limited only by statistical uncertainty (flux-limited). The estimated uncertainties would be one part in 10^4 using the NIST Cold Neutron Research Facility as a neutron source and a running time of 480 hours. This would represent a reduction of the uncertainty of the measurement of τ_β by a factor of 20 over the current value.

In order to provide the full improvement in the neutron lifetime measurement, it is necessary to hold all systematic errors below the level of one part in 10^5. Furthermore, it is necessary to ensure that all technical aspects of the experiment, such as the cooling power provided by the dilution refrigerator, trap depth produced by the magnets, and pulse discrimination provided by the detection mechanisms perform to their design specifications.

Five sources of systematic error have been specifically identified [1]:

1. Absorption of the neutrons by impurities in the superfluid ^{4}He bath, most notably ^{3}He.

2. Inelastic upscattering of the UCN.

3. Delayed escape of neutrons with total energy greater than the trap depth.

4. Losses due to betatron oscillations or Majorana transitions.

5. Loss of neutron decay discrimination due to pulse pile-up.

In this thesis the third item on the list above is considered. Issues related to item 5 and overall signal strength are also considered.

In Chapter 2, numerical simulations of the trajectories of neutrons with initial energies greater than the trap depth are reported. Such neutrons represent a potential

source of error in the measurement of τ_β since they have enough energy to escape the trap but may initially be orbiting in regions where they do not escape. Over time, however, the shape of their orbits may be changed so that they do reach the edge of the trap and escape. One example of such an orbit would be a circular orbit perpendicular to the long axis of the trap, which could decay (due to the non-conservation of angular momentum) into an elliptical orbit. Since the new ellipse's aphelion would be larger than the circular orbit's radius, it is conceivable that the neutron would be unable to escape initially, but would be able to escape after the orbit had changed sufficiently.

The other issue which is addressed in this report is related to discrimination of individual neutron decays using the fluorescence measured by the photodetection electronics. An estimate of the minimum total detection quantum efficiency for the proposed system is 1.3% [5]. Using this estimate, we compute that all neutron decays will result in at least 10 photocathode electrons in the two photodetectors used (one at each end of the trap). An important concern is the time-response of the scintillation and down-converting materials in the system. That is, we want to be sure that neither the helium scintillations nor the down-converting phosphors cause pulse broadening that renders the signal undetectable. Hence we desire a phosphorescent material which delivers visible light in as narrow a pulse as possible, with a minimum decay time for fluorescence. Current investigations by Dr. Golub at the Hahn-Meitner institute are examining the exponential fluorescence decay times for the entire system (helium and phosphor together). In this study we report the time response profiles of three phosphor materials stimulated directly by a UV source.

Chapter 2

Neutron Simulations

2.1 Introduction

As discussed in Chapter 1, one possible source of error in the proposed measurement of the neutron beta-decay lifetime (τ_β) is the delayed escape of those neutrons that have energies greater than the trap depth (E_t). Neutrons with energy higher than E_t should leave the trap in a time short enough so that they escape between the time of their production and the beginning of decay counting (typically 10% of τ_β). If, however, they exist in nearly-stable orbits which bring them to the edge of the trap at some time during the counting period (that is, before they have decayed) then this will result in a systematic error in the determination of τ_β.

We define the depth of the magnetic trap as being the minimum energy necessary for a particle within the trap to escape. Strictly speaking, this exists only at an infinitesimally small point (or perhaps several points) on the edge of the trap. For any given neutron energy greater than the trap depth, there exists a finite accessible surface area of the cell wall at which the neutron can escape. (It is assumed that when the neutron hits the physical wall it is lost.) In practice, this region of possible escape is usually localized to one or two contiguous areas of the cell wall. A particle with energy sufficient to escape will in fact spend some time traversing the trap before it encounters the escape region. It is even possible that the neutron will never encounter the escape region before it beta-decays.

The simulations in this chapter are concerned with ascertaining the escape times of neutrons with energies greater than the trap depth. Using several different trap shapes and a range of neutron energies, we have carried out Monte Carlo simulations which trace the trajectories of neutrons with random initial conditions. These simulations determine when the neutrons escape from the trap, up to some maximum time.

2.2 Methods

2.2.1 Computer Modeling

The computer procedure being performed in the generation of neutron trajectories is the integration of the differential equations of motion. We assume that the neutron is moving at a speed slow enough for its magnetic moment to be constantly aligned with the external magnetic field. The potential energy at any time is given by $U = \mu|\vec{B}(\vec{r})|$ where μ is the magnetic moment of the neutron and $|\vec{B}(\vec{r})|$ is the magnitude of the magnetic field at $\vec{r}$. With this simplification, the process for determining the motion of the neutron requires only the solution of $\vec{F} = m\vec{a}$:

$$\begin{aligned} m\frac{d^2x}{dt^2} &= -\frac{\partial(\mu B(x,y,z))}{\partial x} \\ m\frac{d^2y}{dt^2} &= -\frac{\partial(\mu B(x,y,z))}{\partial y} \\ m\frac{d^2z}{dt^2} &= -\frac{\partial(\mu B(x,y,z))}{\partial z} \end{aligned}$$

To solve these differential equations we must be able to compute the gradient of the magnitude of the magnetic field at any point in space. This procedure is handled in two steps. Prior to computing any trajectories a trap geometry is chosen and a program is used to compute the magnitude of the magnetic field generated by the given arrangement of solenoids and current bars at each of the points lying on a three dimensional cartesian grid which encompasses the trap region. A grid of 100 points in each orthogonal direction is typical. The magnetic field magnitudes are computed

from the Biot-Savart law using Romberg integration [8, pages 140–141].

The array of magnetic field magnitudes (the "potential grid") is then used as an input to the trajectory program. For each individual trajectory, the program chooses random initial conditions. The choice is made in steps. First, the total energy of the new particle is chosen at random from within a range of energies specified by the user. Second, the particle is placed at a random location within the trap. (The mean free path of an 8.9 Å neutron is approximately 100 m, much larger than the dimensions of the trap, so UCN production is expected to be spatially uniform throughout the trap region [1].) The particle's potential energy at this point is computed by bilinear interpolation on the potential grid [8, pages 123ff]. Third, the kinetic energy is computed as the difference between the potential and total energies. Fourth and finally, initial velocities are assigned by assigning the kinetic energy to a random direction.

Given the randomly determined initial conditions, computation of the trajectory proceeds by implementing an adaptive stepsize integrator. The step used is a "quality-controlled" Cash-Karp Runge-Kutta step [8, pages 714–722]. For each time step Δt, a new position and velocity are computed as follows:

$$\begin{aligned} x_{n+1} &= x_n + vx_n \Delta t \quad & vx_{n+1} &= vx_n - \tfrac{1}{m}\tfrac{\partial(\mu B(x,y,z))}{\partial x} \\ y_{n+1} &= y_n + vy_n \Delta t \quad & vy_{n+1} &= vy_n - \tfrac{1}{m}\tfrac{\partial(\mu B(x,y,z))}{\partial y} \\ z_{n+1} &= z_n + vz_n \Delta t \quad & vz_{n+1} &= vz_n - \tfrac{1}{m}\tfrac{\partial(\mu B(x,y,z))}{\partial z} \end{aligned}$$

For each time step, the partial derivatives of the potential function for the current location are computed using Ridders' method of polynomial extrapolation [8, page 188]. This algorithm requires a continuous function as its input, and hence we use the bilinear interpolation on the potential grid, as described above. The program then iteratively solves the differential equations in the manner described for a length of time specified by the user, generating a trajectory composed of discrete steps. In our simulations, we compute trajectories until either the neutron reaches the trap walls (where it would be absorbed and lost) or until some maximum time has elapsed.

2.2.2 Trap Design

In this study of neutron trajectories, two basic trap designs have been used. The first is a quadrupole trap similar to that used in the MIT spin-polarized hydrogen trap [9]. In this design, neutrons are confined radially using a quadrupole field and axially by solenoid pinch coils. The current in the two pinch coils at either end of the trap runs in the same direction. Additional solenoid coils (bucking coils), with opposite current direction to the pinch coils, are used to steepen the field gradient in the axial direction at the edge of the trap. The specific magnet configuration used was based on preliminary designs for the first neutron trap. The trap has a total length of 54.6 cm and a radius of 1.41 cm. Figure 2-1 shows the design of the quadrupole trap and the magnetic field profile along the trap axis. Figure 2-2 shows the magnetic field profile (in Gauss) for a slice perpendicular to the trap axis. The standard current densities used in these computations were 35,000 Amps/cm^2 in the quadrupoles and 50,000 Amps/cm^2 in the solenoids (these current densities are typical for NbTi superconducting coils in this field range). For these parameters, the trap depth is 1.5 Tesla. Two variants of this trap were also considered. In one, the trap was identical except that one quadrupole carried only 70% (24,500 Amps/cm^2) of the current carried by the others. In the other, an extra current bar was introduced along the diameter of one of the pinch solenoids. These traps had depth 11327 gauss and 15020 gauss respectively. In all cases, the minimum field magnitude was located at the intersection of the trap edge with two planes, each perpendicular to the axis of the trap and passing through the center of one of the bucking coils.

A second class of trap design was also considered. This trap consists of identical solenoids arrayed along the axis of symmetry. Neighboring solenoids carry current in opposite directions. Hence the trap can be thought of as a sequence of anti-helmholtz traps, and is referred to as the "multi-helmholtz" trap below. The solenoids used each had a current density of 50,000 Amps/cm^2, an inner radius of 4.353 cm and an outer radius of 4.736 cm, a length of 8.89 cm, and a center to center separation of 10 cm. Figure 2-3 shows the magnetic field profile along the axis (the dark portions are

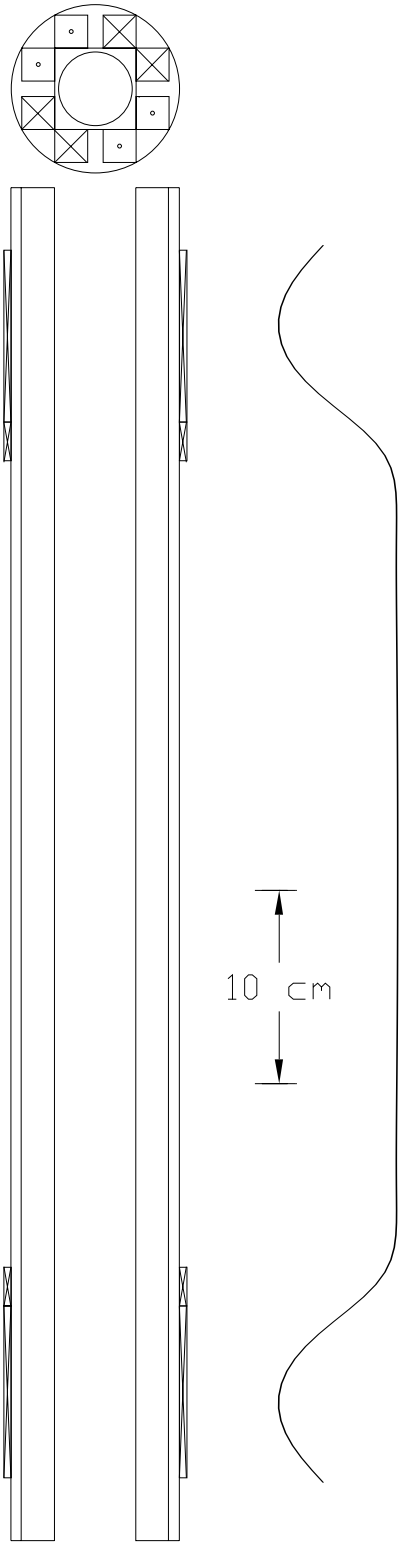

Figure 2-1: The quadrupole trap design is presented. Both a view parallel to the trap axis and a slice perpendicular to it are shown. Below the trap, the magnetic field profile along the trap axis is shown.

Figure 2-2: The magnitude of the magnetic field (in Gauss) is shown for a slice through the center of the trap, perpendicular to the trap axis.

Figure 2-3: Magnetic field magnitude (Gauss) of the multi-helmholtz trap in a slice parallel to the trap axis.

the solenoids themselves). The trap configuration can also be seen from this figure since the dark rectangles at the figure's edge indicate the positions of the solenoids.

2.3 Results

2.3.1 Multi-Helmholtz

Initial studies were performed using only one anti-helmholtz trap. The general form of the trajectories observed seem to be precessing elliptical orbits inclined out of the x-y plane (taking the z axis as the axis of symmetry). The projection of the motion

onto the x-y plane is that of elliptical orbits precessing, as is seen in Figure 2-4. The motion in the z direction is more difficult to identify, but appears consistent with the notion of a rapidly precessing elliptical orbit.

One analysis performed was to average the energy in each direction in a sliding window. The sliding window's time width was taken to be the length of time needed for a typical trajectory to complete 10 orbits. This analysis indicated that while the average energy in the z direction is constant, the energy in the x-y plane oscillates between the x and y directions. This oscillation displays a sinusoidal form with period approximately equal to the time-averaging window's width, as can be seen in Figure 2-5. This type of behavior appears in all cylindrically-symmetric systems studied and is the result of conservation of angular momentum in the axial direction.

In the case of multiple anti-helmholtz coils, the qualitative behavior of the orbits is relatively the same. The simplest orbits remain within one anti-helmholtz pair, behaving as if in a standard anti-helmholtz trap. Some orbits which start with high energy in the axial direction spend some time moving between the various subtraps before eventually localizing in one. Since the localization in one trap is representative of a transfer of energy from the axial to radial direction, it is usually followed shortly by the escape of the particle from the trap, since the radius of its orbit has thus increased to a size where it can escape.

In examining the individual trajectories of a particle localized in a particular anti-helmholtz pair, it appears that all of the trajectories assume some sort of precessing elliptical orbit. Hence, those that escape immediately are ones whose aphelion is located outside of the trap for the initial orientation of the orbital ellipse. For other orbits, the far point of the particle's orbit does not reach outside of the trap until the orbit has precessed for a while. In yet other cases, particles have been seen to achieve very stable orbits which remain within the trap for as long as 100 seconds.

Our primary goal was to obtain a profile of the escape time as a function of energy of the trapped neutrons. To this end, several energy bands have been investigated. Table 2.1 shows the percentage of neutrons in each energy band which escaped the trap in 100 seconds or less. Table 2.2 shows the same information for a maximum

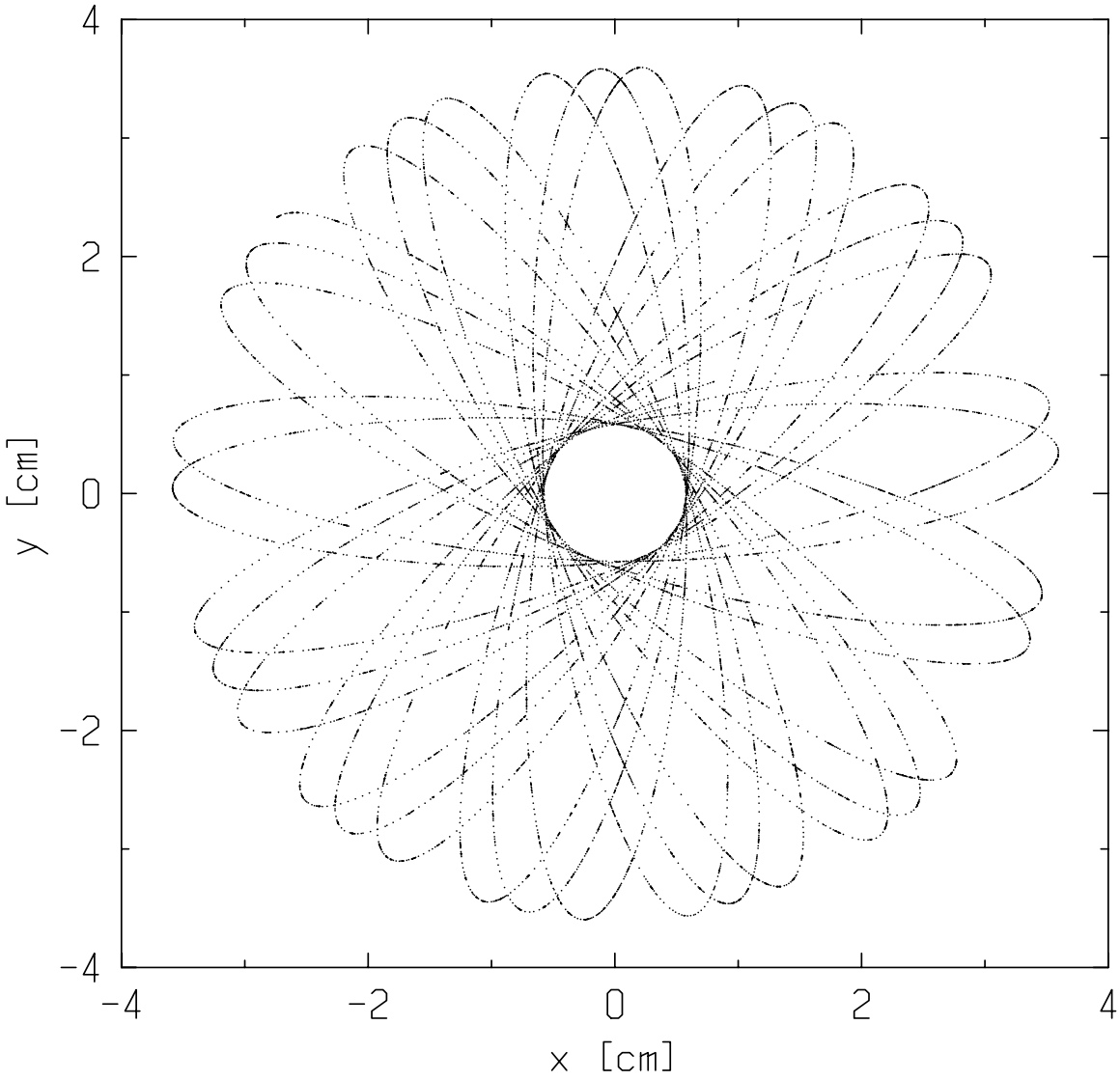

Figure 2-4: Projection onto the x-y plane of the motion of a typical trajectory in the anti-helmholtz trap.

Neutron Energy Band	N_{traj}	% escaped in 100 s	Max Escape Time
104-105	100	14	44.5
109-110	100	28	82.6
119-120	432	86.8	89.3
190-200	1100	100	0.0727

Table 2.1: Trap escape rates for neutrons of various energies from the multi-helmholtz trap to escape in 100 seconds or less. Neutron energies are represented as a percentage of the trap depth. N_{traj} is the number of trajectories computed.

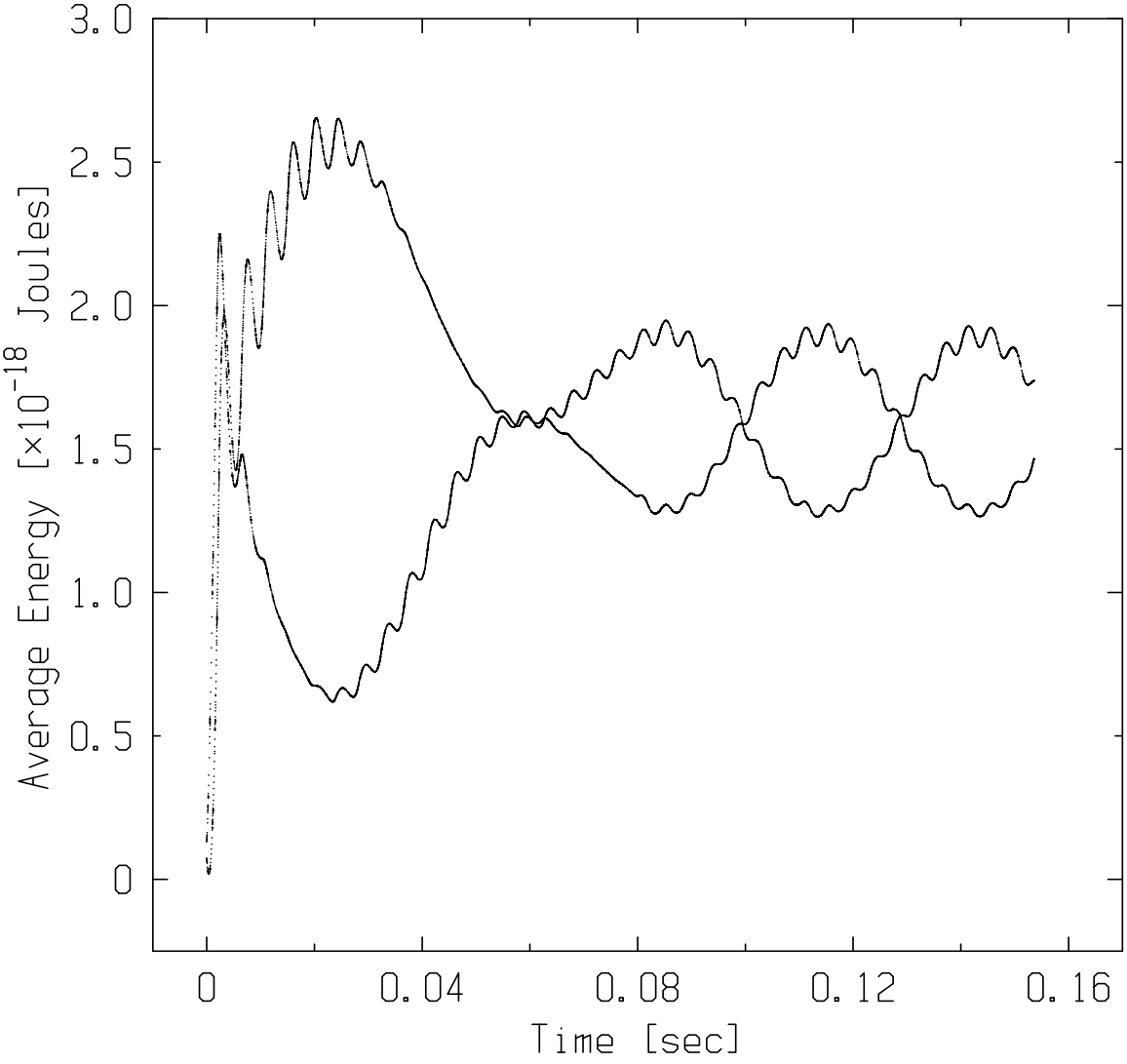

Figure 2-5: Average x and y directional energies for an anti-helmholtz trap (parallel to the z axis).

Neutron Energy Band	N_{traj}	% escaped in 10 s	Max Escape Time
104-105	100	9	5.85
109-110	100	21	9.62
119-120	100	73	9.58

Table 2.2: Trap escape rates for neutrons of various energies from the multi-helmholtz trap to escape in 10 seconds or less. Neutron energies are represented as a percentage of the trap depth. N_{traj} is the number of trajectories computed.

escape time of 10 seconds. Figure 2-6 shows histograms of the escape times for each of the trajectory runs shown in Tables 2.1 and 2.1. It appears that the escape times follow an exponential or power law distribution. Furthermore, we can say to a certainty of at least one part in 10^3 that neutrons with energy 190-200% of the trap depth will escape in less than 1 second.

2.3.2 Quadrupole

The quadrupole trap was studied in the same manner as the multi-helmholtz trap. That is, a qualitative analysis of the trajectory types was performed, and escape statistics were generated through Monte Carlo simulations.

The orbits in the quadrupole trap mainly look like precessing lissajous figures in their projection onto the x-y plane. In addition to this motion, the neutrons also "bounce" between the endcaps. The neutrons take about 0.4 s to travel between the endcaps. Upon each encounter with the endcap, the x-y precession shifts and a new lissajous figure is formed. Figure 2-7 shows a projection of a typical trajectory onto the x-y plane, while Fig 2-8 shows the same trajectory projected onto the x-z axis. Unlike the multi-helmholtz, where the escape time can be thought of as a result of precession, the quadrupole trap's escape time is not so easy to mentally characterize. It seems as though modification of the endcap shape might affect the degree of "randomization" which the trajectory undergoes at the end of each axial pass.

Just as for the multi-helmholtz trap, the escape times (up to some maximum) have been determined for each trajectory in the simulation. Table 2.3 reports the number of particles that escaped in 10 seconds or less of trajectory time. Table 2.4

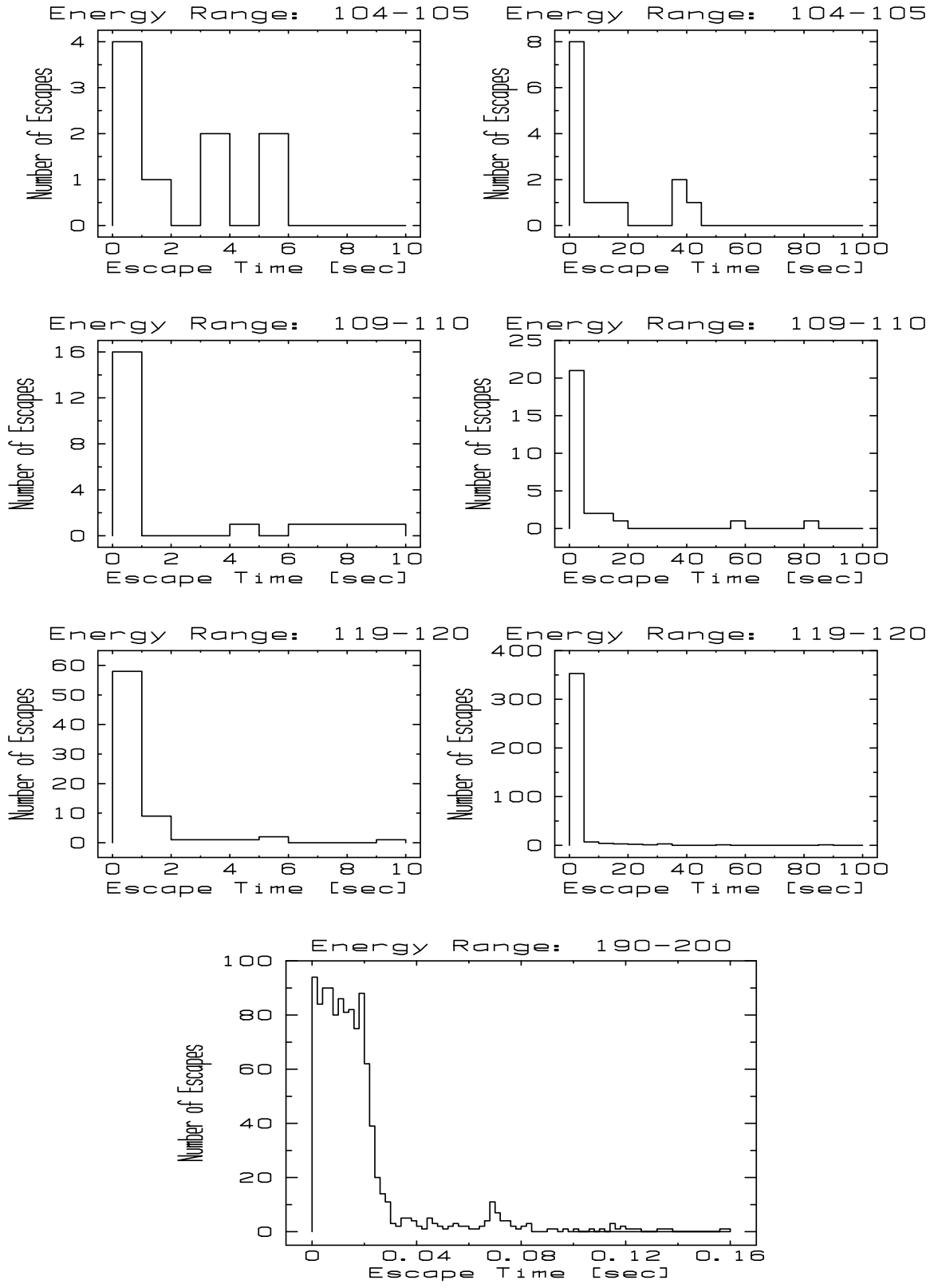

Figure 2-6: Histograms of the escape times of neutron trajectories from the multi-helmholtz trap. A variety of energies are shown. The maximum time length is either 10 seconds or 100 seconds.

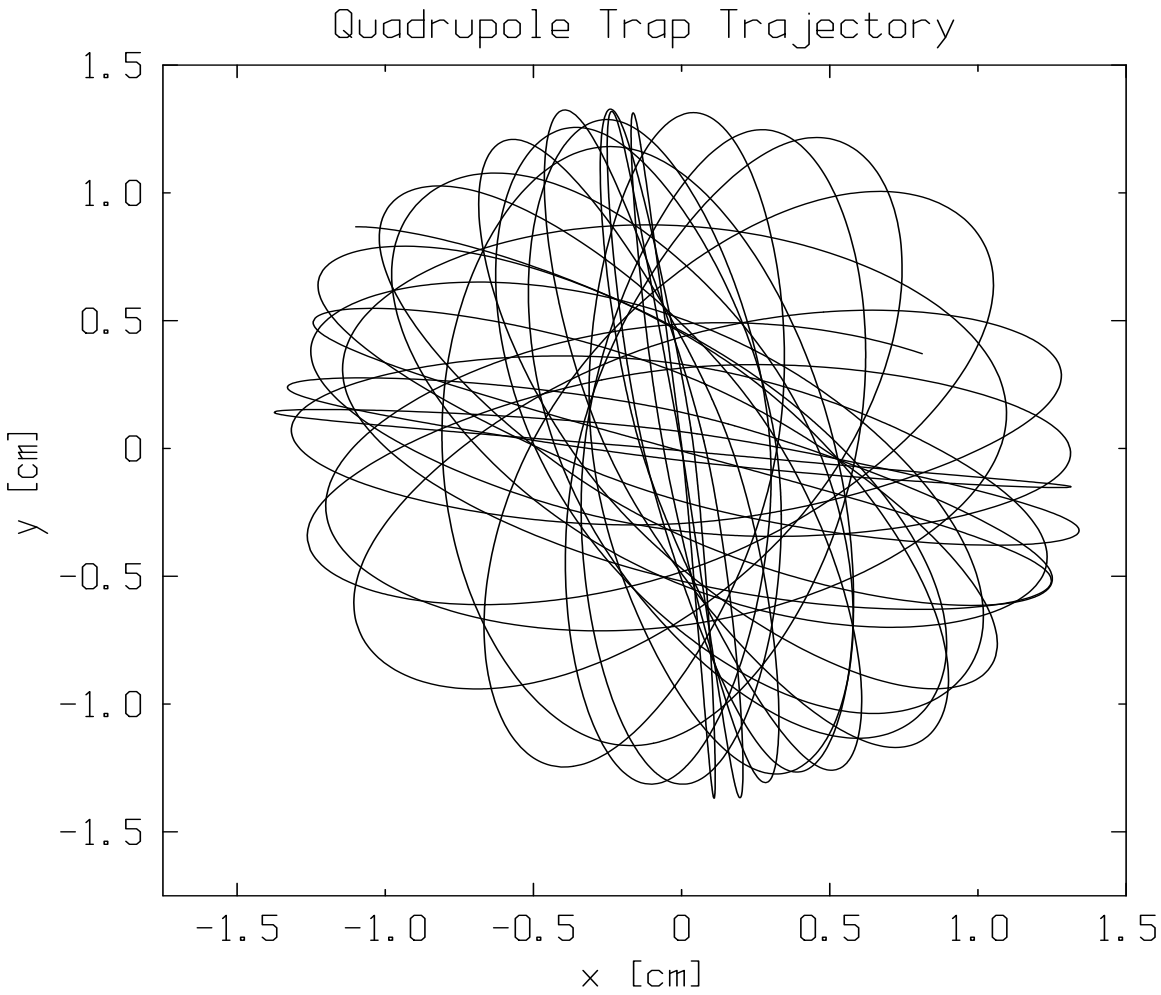

Figure 2-7: Projection of a typical trajectory in the quadrupole trap onto the x-y plane. The total running time of the simulation is 0.6 seconds.

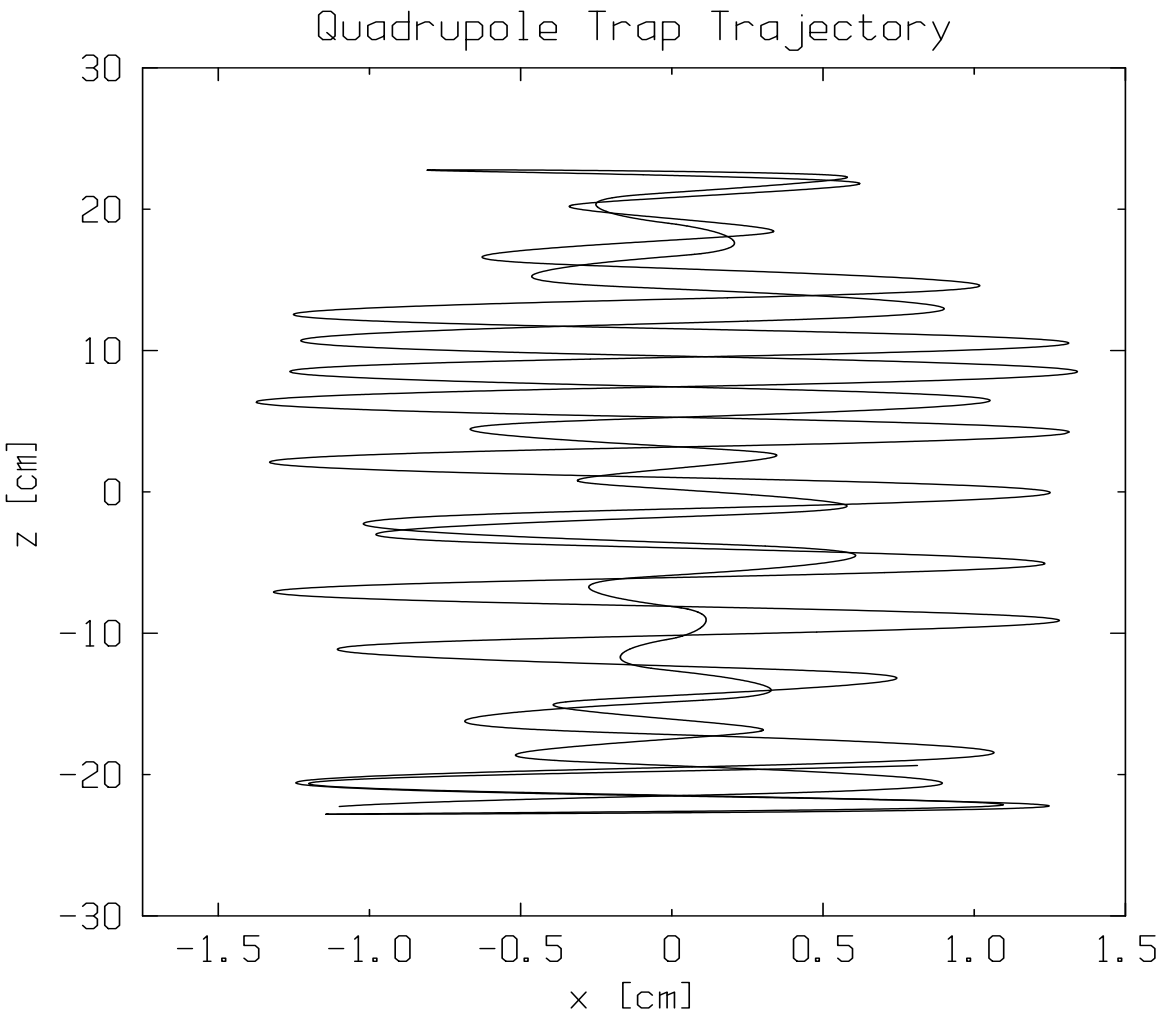

Figure 2-8: Projection of a typical trajectory in the quadrupole trap onto the x-z plane. The total running time of the simulation is 0.6 seconds. The trajectory is the same as that in Figure2-7

Trap	Energy Band	% escaped in 10 s	Max Escape Time
a	104-105	55	9.36
a	109-110	64.5	9.39
a	119-120	82	5.74
b	104-105	42	9.84
b	109-110	54	9.01
b	119-120	78	8.77
c	104-105	49	9.27
c	109-110	66	8.66
c	119-120	76	5.79

Table 2.3: Trap escape rates for neutrons of various energies from the three quadrupole traps to escape in 10 seconds or less. Trap a is the standard quadrupole trap. Trap b has one coil turned down to 70% of its full strength. Trap c is a standard quadrupole trap with an extra bar running along the diameter of the endcap. Neutron energies are represented as a percentage of the trap depth. For all of the statistics reported here, 100 trajectories were computed.

Trap	Energy Band	N_{traj}	% escaped in 100 s	Max Escape Time
a	104-105	25	72.0	56.59
a	109-110	44	88.6	35.34
a	119-120	58	93.1	92.02
c	104-105	28	75.0	65.83
c	119-120	64	92.2	99.04

Table 2.4: Trap escape rates for neutrons of various energies from the three quadrupole traps to escape in 100 seconds or less. Trap a is the standard quadrupole trap. Trap c is Trap a with an extra bar running along the diameter of the endcap. Neutron energies are represented as a percentage of the trap depth. N_{traj} is the number of trajectories computed.

reports escape rates for a maximum time of 100 seconds.

We have computed escape times for three trap configurations, as described above. The trap with one coil turned down was studied in the hopes that this change would introduce more "convexity" into the potential, as well as breaking the symmetry of the trap. The trap with the additional current bar through the endcap was studied in order to see how a change in the endcap shape would affect the rate of escapes. In each of the traps, we have considered the effect of gravity as a symmetry-removing element, by rotating the trap so that the angle between the gravitational field and the line connecting one of the pairs of quadrupoles is $\sqrt{2}/\pi$ radians.

Histograms of the escape time profiles for the quadrupole traps are substantially

similar to those for the multi-helmholtz trap. In all cases where enough simulations have been completed to be statistically significant, we can claim that better than 90% of the trajectories in the 119-120% energy band escape in the first second. However, the number of neutrons which escape in more than 10 and less than 100 seconds and the number of neutrons not escaping in the first 100 seconds are both greater than 1%, much less one part in 10^5.

2.3.3 Billiard Systems

In order to study the impact of convexity on the ergodicity of trajectories, a hard-walled, "billiard" system was studied. In this theoretical system, the particles bounce perfectly elastically off of a hard surface.

The system which was chosen for study consists of the space between the intersection of six spheres. Figure 2-9 shows the general shape of the system. In order to study the impact of convexity, the system was chosen so that a single parameter could be varied in order to adjust the convexity of the system. The space in which the "billiard ball" bounces is taken as the space between six spheres, each centered r away from the origin along one of the cartesian axes, with radius $R^2 = r^2 - \sqrt{2}r + 1$. It is important to note that the spheres always (independent of R) intersect at the corners of a cube of edge 2 centered at the origin (that is, at (0,0,1), (0,1,0), and so on). Thus, as R decreases, the region in which the billiard can move becomes more and more convex as it stretches from some small area in the middle along eight spikes out towards the cube's corners.

As a measure of the ergodicity of the system, the Lyapunov exponent was computed using Monte Carlo simulations. The Lyapunov exponent reflects the rate at which trajectories which are initially close in phase space move apart over time [10][11]. The Lyapunov exponent after n time steps is computed as

$$K_n = \frac{1}{n\tau} \sum_{j=1}^{n} \ln \frac{d_j}{d_0}$$

where d_j is the distance in phase space between the two trajectories after j steps.

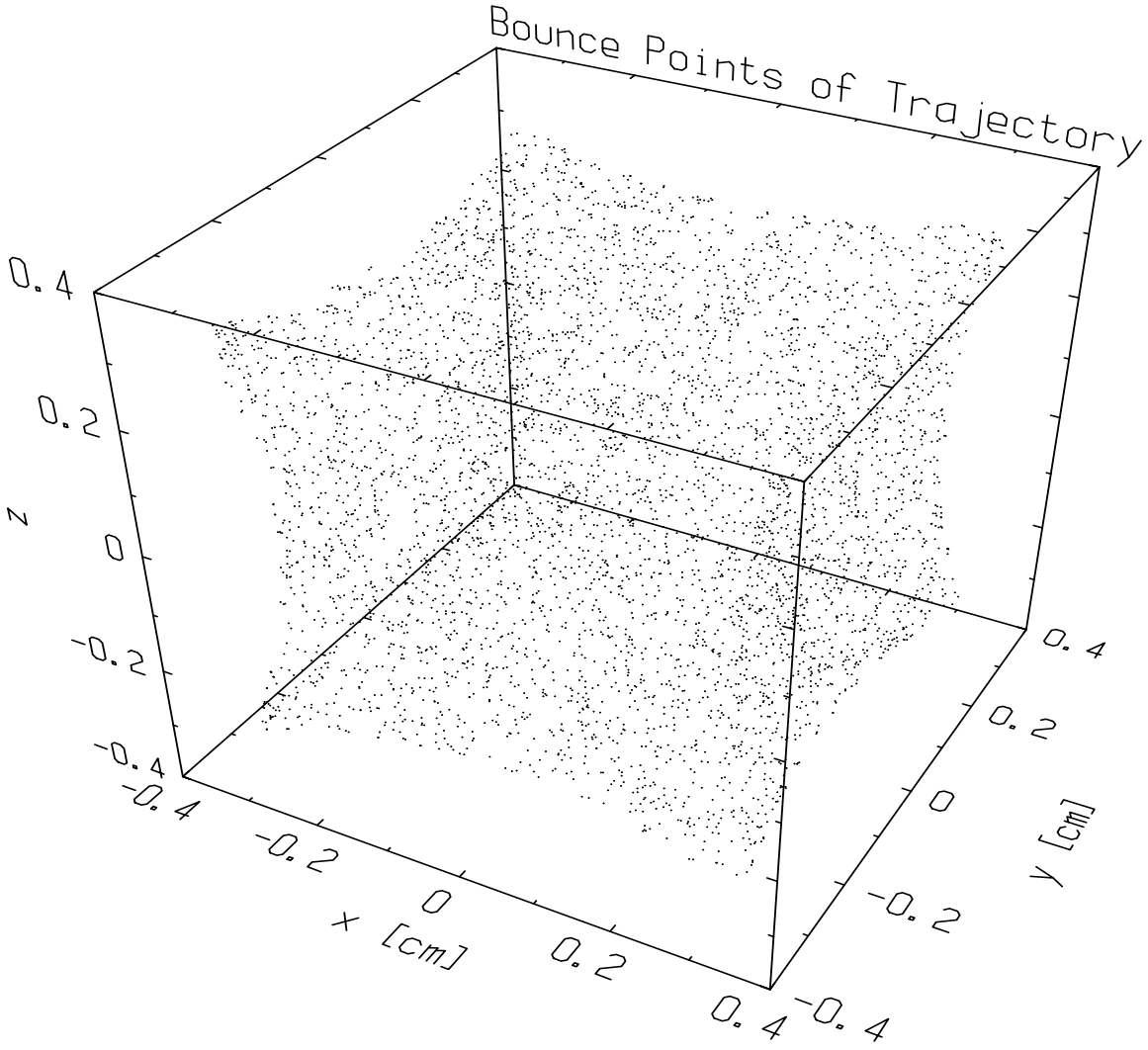

Figure 2-9: The shape of the convex surface studied as a billiard system. The dots are the points at which one trajectory bounced off of the walls of the system.

In order to prevent the value of the Lyapunov exponent from saturating over time, one of the two trajectories is renormalized after each time step, so that the distance between the two in phase space is set to be $\vec{d}_j/d_0$.

Figure 2-10 demonstrates the relationship between R and the Lyapunov exponent for the system. Since R determines the convexity of the system, this is a comparison of the effect of convexity on ergodicity. As we expect, the Lyapunov exponent is larger as R decreases (and hence the convexity of the system is increasing since the area carved out between the spheres is decreasing). In the limit of $R \to \infty$, the billiard system becomes a cube, which is a completely non-ergodic system, as reflected in the approach of the Lyapunov exponent to 0. It is interesting to note that the Lyapunov exponent appears to have a power law relationship with R, with a fractal dimension of approximately 5. Thus, this small study substantiates the positive correlation between convexity in the shape of a system's walls and the degree of ergodicity of the trajectories in it. This suggests that one way to make the trajectories in neutron traps more ergodic would be to introduce more convexity into the system, either through "convex" magnetic potentials, or by the introduction of a physical element with convex shape.

2.4 Discussion and Conclusions

The simulations which have been conducted to date suggest that for the trap designs studied the delayed escape of neutrons with energy higher than the trap depth would occur at a rate higher than is acceptable for the desired accuracy of our neutron lifetime measurement. This situation is observed in both the quadrupole traps and the multi-helmholtz configuration. In both cases, more than one percent of the neutrons with energy 119-120% of the trap depth escape at some intermediate time between 10 and 100 seconds. This suggests that during the lifetime of the neutron (887s) a significant number of marginally trapped neutrons could escape

Having verified that the delayed escape of energetic neutrons has the potential to corrupt our counting statistics, it is worthwhile considering possible future steps to

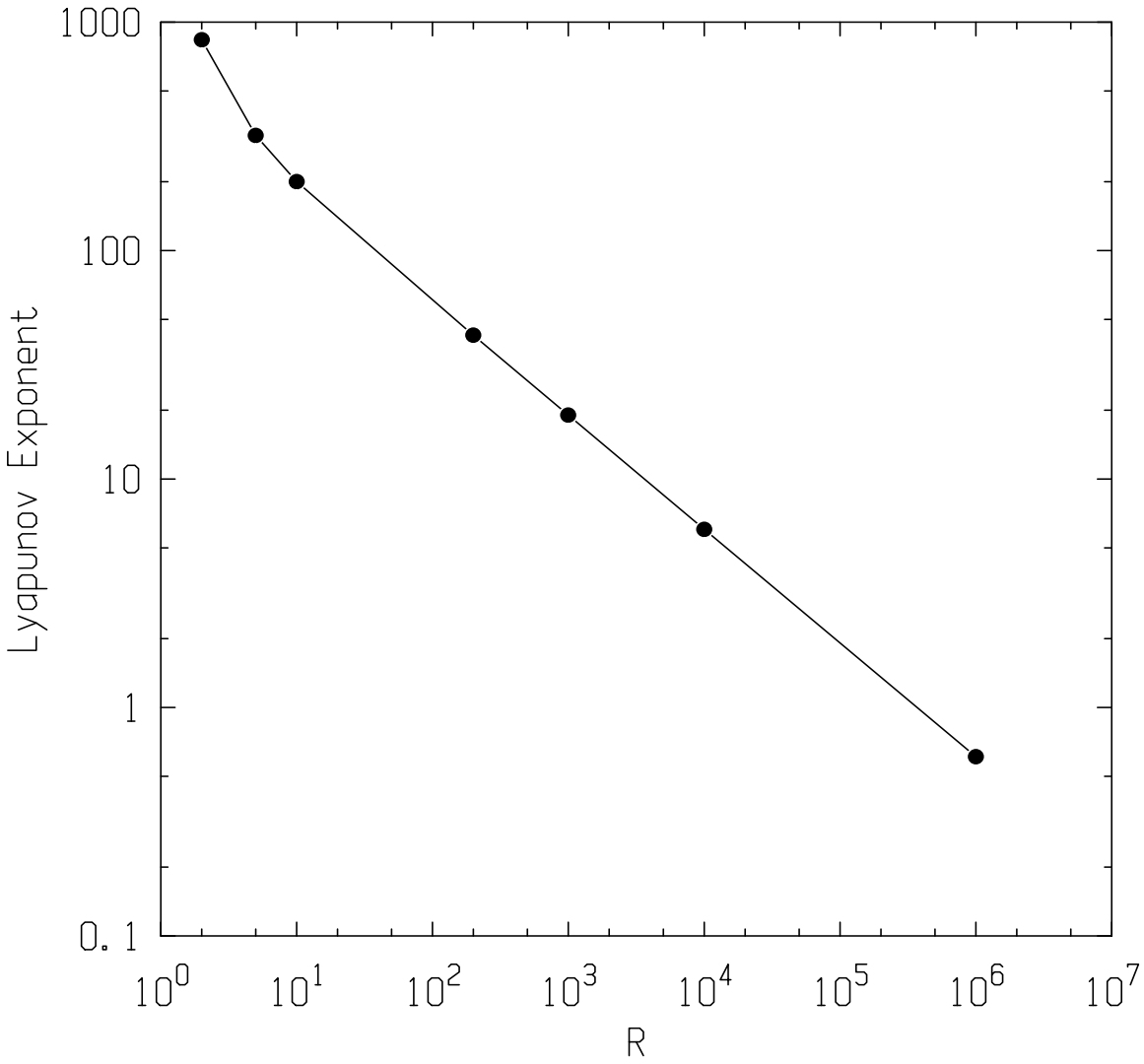

Figure 2-10: Lyapunov exponents as a function of R, the radius of the spheres defining the region in which the billiard can bounce. Hence, a measurement of the relationship between convexity and ergodicity.

counteract the problem. As a first step, additional simulations covering more energy bands and longer maximum times should allow a more accurate determination of the fraction of neutrons at each energy level which escape in an intermediate time (more than 10 and less than 1000 seconds).

In addition to enhancing our understanding of the problem of delayed neutron escapes, future work should focus on developing experimental techniques to counteract the problem. There are two approaches to this method. The first approach would be to modify the trap in some way to enhance the escape rate of neutrons with energy higher than the trap depth. As the current work has shown, several simple modifications of the quadrupole trap did not lead to any improvement in its escape rates. More complicated methods, such as modulating the magnetic field at the edge of the trap with an RF field, or physically introducing some hard convex object (like the billiard systems' walls) into the trap, might be of some value.

An alternate approach would focus on detecting all neutrons which escape from the trap, rather than trying to modify the trap's escape rates. One possibility would be to use lithium-doped films in the cell lining which would absorb neutrons and emit visible light. By pulse height and width discrimination, such light should be discernible from the light output by the fluorescent materials due to beta-decay (discussed in the next chapter). Further research should be devoted to testing the applicability of such lithium-doped films to this problem.

In summary, we have discovered that the delayed escape of neutrons with energies higher than the trap depth represents a potential barrier to achieving the statistical accuracy desired for the proposed measurement of the neutron lifetime. Further work should be devoted to more precisely specifying the energy-time dependence of trap escape rates. Experimental methods of facilitating neutron escape or detecting delayed escapes should be pursued.

Chapter 3

Ultraviolet Down-converting Materials

3.1 Setup and Procedure

3.1.1 Introduction

Fluorescent materials for down-converting ultraviolet to visible light are part of the proposed scheme for counting neutron decay events. By using down-converting materials, we can take advantage of the wide body of standard techniques for piping and detecting the visible light produced. It is estimated that in each of the two phototubes used for detection, 10 photoelectrons will be measured per decay event (See Chapter 1, Figure 1-1, and [5]). Due to the relatively low number of detectable photons per decay, we must ensure that any broadening of the light pulse used for detection (due to fluorescent decay times in the ^{4}He scintillation or the down-converting materials) will not adversely affect our signal. As part of the effort to determine the effect that fluorescent beta-decay times will have on the decay signal, this chapter reports an experiment to study the fluorescent decay behavior of three potential down-converting materials at room temperature and at low temperature (4K).

3.1.2 Down-converting Materials

The decay times of three fluorescent materials were studied. Figure 3-1 shows the chemical structures of the three compounds: sodium salicylate (NaSal), 1,1,4,4,-tetraphenyl-1,3-butadiene (TPB), and trans-p,p'- diphenylstilbene (DPS). These fluorescent materials convert ultraviolet light to visible light over a broad range of input frequencies. Figure 3-2 (from [12]) shows the relative quantum efficiencies of all of the fluorescent materials considered over a range from 180-400 nm. Although not shown, the same paper reports a flat absorption curve down to 50 nm for DPS and TPB. All of the downconverters emit over a broad range in the visible spectrum. TPB, for example, has a peak emission at 428 nm with emission from 390 to 530 nm [13]. Figure 3-3 shows the emission spectra of TPB and NaSal.

Samson notes that many different values of absolute quantum efficiency have been reported for sodium salicylate and recommends a value of 65% for the range of 40–340 nm [14]. DPS is reported to have a relative quantum efficiency of roughly twice that of NaSal in the range 60–250 nm [14]. Carolan and Manley report absolute quantum efficiencies for TPB which increase from 100% at 350 nm up to 300% at 1 nm [15]. In the regime of our operation, the absolute quantum efficiency of TPB is approximately 200%. Samson also reports the fluorescent decay times at room temperature for NaSal and DPS as 7-12 ns and 6 ns, respectively. [14].

Acrylic films doped with the down-converting material were prepared and coated onto a polycarbonate substrate. The acrylic resin was prepared from Dupont "Elvacite" (poly-methyl methacrylate, PMMA) dissolved in Toluene at a concentration of 10% by weight. The down-converting materials were each dissolved into acrylic resin at a concentration of 1% of the Toluene weight. The method of preparing doped acrylic resins and suggestions for maximizing conversion efficiency by selecting appropriate acrylic and fluorescent material concentrations is taken from similar work done by Viehmann and Frost [16]. Slides of approximately 1 cm $\times$ 1 cm of polycarbonate plastic (Lexan) were used as the substrate. The slides were 0.04 inches (1.0 mm) thick.

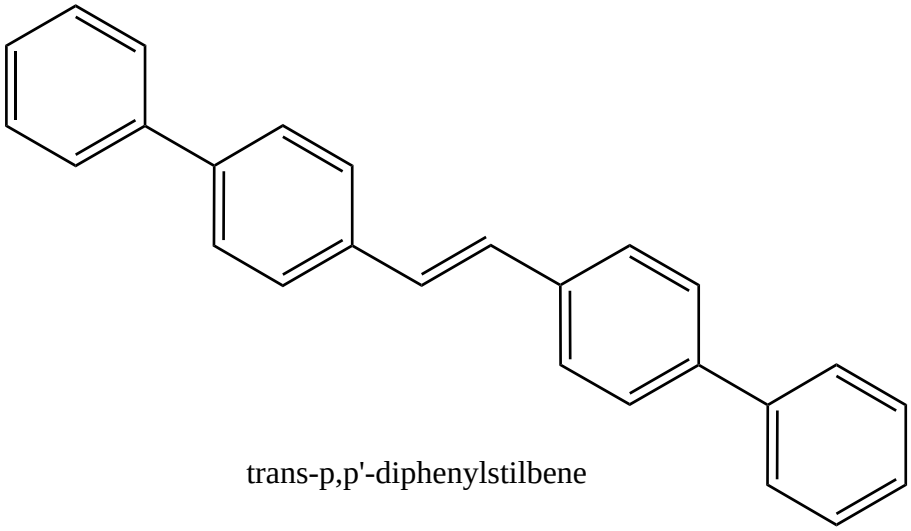

trans-p,p'-diphenylstilbene

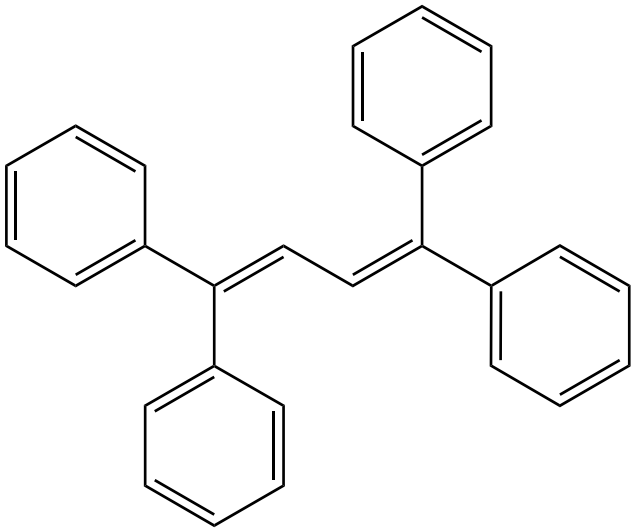

1,1,4,4-tetraphenyl-1,3-butadiene

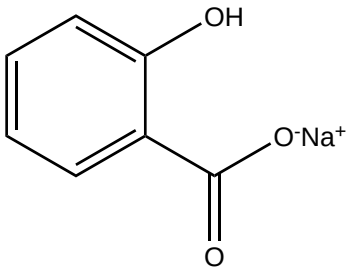

Sodium Salycilate

Figure 3-1: The chemical structures of the three fluorescent materials studied: sodium salicylate, 1,1,4,4,-tetraphenyl-1,3-butadiene, and trans-p,p'- diphenylstilbene.

Figure 3-2: Relative quantum efficiencies of several fluorescent materials. From Mai and Drouin (1971) [12, Figure 1]

Figure 3-3: Emission spectrum for TPB and NaSal. Left: TPB, from Burton and Powell (1973) [13, Figure 2]. Right: NaSal from Samson (1967) [14, Fig. 7.4]

Material	Weight Before (g)	Weight After (g)	Area (cm^2)	Thickness (mg/cm^2)
PMMA (blank)	0.77	0.80	6.2	4.8
TPB	0.44	0.50	5.1	12
NaSal	0.61	0.50	4.1	???
DPS	0.59	0.60	5.1	2.0

Table 3.1: Thicknesses of the four sample films used. The estimated error in the measurement of the weights is ± 0.02 g.

The downconverter-containing resins were coated onto one side of the polycarbonate slides by holding the slides at a slight angle from the vertical and dripping the resin from a Pasteur pipette onto the upper edge of the slide. The resin thus flowed over the entire surface of the slide, with excess running off of the bottom. Typically only one pass along the top of the slide was made so that the film would be as thin as possible. Table 3.1 shows the thickness of the coatings applied (in mg/cm^2) for each of the films used in the experiment.

Film thicknesses were determined by weighing the slides before and after application of the films. Due to the method of application, one would expect the films to be of uneven thickness over the area of the slide (with the films thicker at the edge which was at the bottom during application), however since the UV beam was tightly focused on the middle of the sample, it interacted with an area of locally-uniform thickness. Furthermore, that thickness should be about the average thickness of the film over the entire slide.

3.1.3 Apparatus

An overview of the experimental apparatus used is shown in Figure 3-4. A continuous-wave 243 nm beam was chopped with a mechanical chopper and focused onto slides coated with phosphor-doped PMMA. The slides were contained in a small cryostat with windows (either at room temperature or approximately 4 K in this experiment). The fluorescence of these materials was detected by a photomultiplier.

The 243 nm beam used is generated by doubling the output of a CW laser. The 486 nm source is produced from a Coherent 699-21 ring laser (using a Coumarin 102 dye jet) pumped by a Coherent I-200 krypton ion laser. A tellurium reference

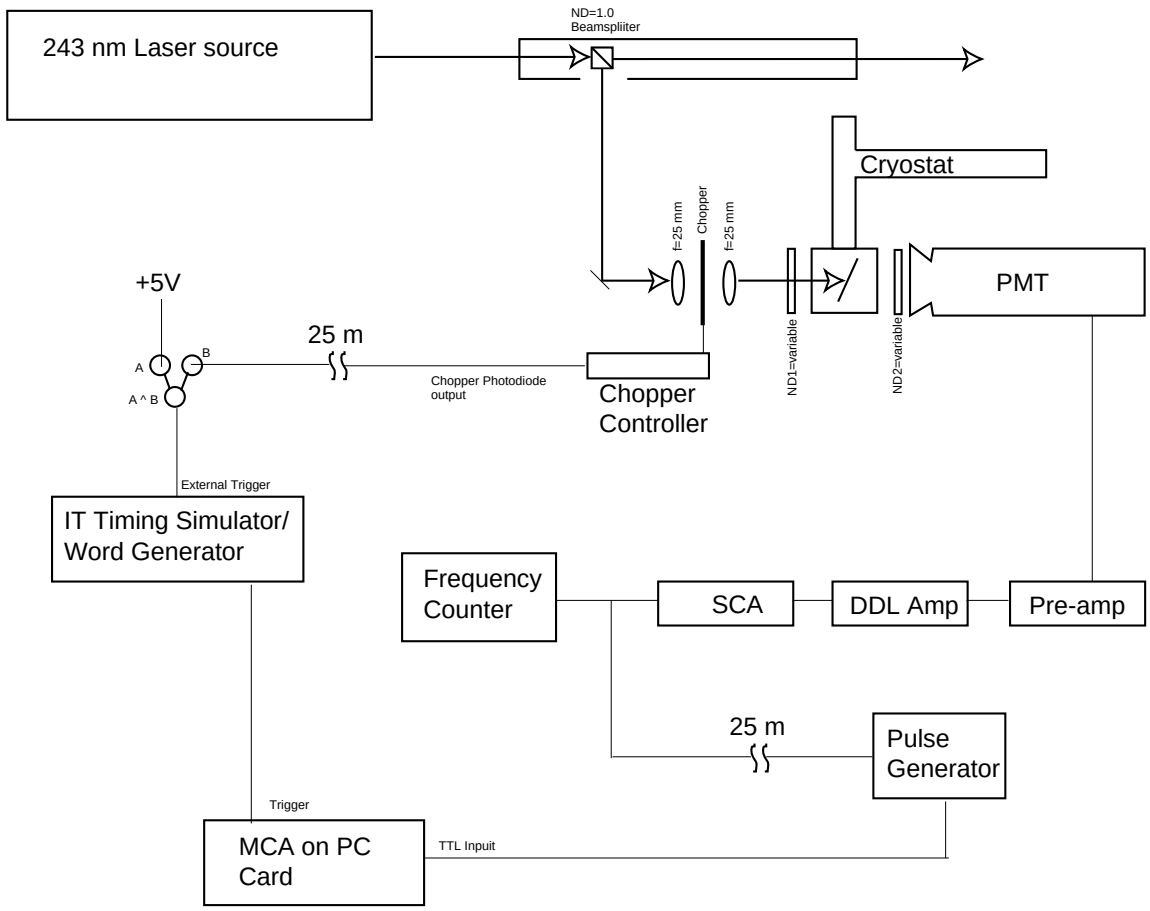

Figure 3-4: Experimental setup used for testing the fluorescent decay time of ultra-violet down-converting materials.

spectrometer provides a frequency reference for the 486 nm laser. Frequency doubling of the dye laser output is accomplished through second harmonic generation in a beta-barium borate crystal [17, Chapter 4].

The beam used in this work was split from the output beam using a neutral density filter (ND=1.0). The remaining 10% of the beam was left over for use in other experiments (90% of the beam was reflected to the table). Constant alignment of the beam was maintained by comparing the transmitted 10% of the beam to an alignment standard. The beam's power was monitored and adjusted throughout the course of the experiment to maintain a roughly uniform power over time (within 20%). A typical beam power as measured by a photodiode placed on the table immediately in front of the cryostat was 0.2 mW.

The beam was chopped by placing a mechanical chopper (SRS Model SR540 chopper-controller) at the focal point of an f=25 mm UV-grade fused-silica lens. The overall beam shape was maintained by placing a second, identical lens in a symmetric position with respect to the chopper, in a "telescope" arrangement. For all of the measurements reported below, the chopper was operated at a nominal rate of 10 Hz. The chopper contained an internal photodiode to feedback and control the chopper at the appropriate rate. The signal from this photodiode was also output by the chopper's controller. Observation of this signal allowed both a more accurate measurement of the exact chopping rate, and a triggering signal for the counting electronics, which were set to repeatedly count in some portion of the chopper's period over a time scale of many triggers.

The sample slide was held inside of a Liquid Transfer Helitran Refrigerator (Air Products and Chemicals Model LT-3-100) cryostat. This cryostat was evacuated to a pressure of less than 1 millitorr throughout operation, both at room temperature and at 4K. The vacuum was maintained by a mechanical pump with a liquid nitrogen cold trap (to prevent pump oil from entering the cryostat). Optical access to the entire vacuum system was provided by two Corning 7940 fused silica windows, one on the beam-side and one on the PMT side.

For low temperature operation, the metal tip to which the sample was clamped

was cooled by the flow of cold helium gas (generated by the evaporation of liquid helium) through the transfer tip portion of the helitran. The temperature of the system was measured using a diode thermometer located slightly up the cooling arm from the film samples. Although the calibration curve of the diode thermometer did not extend below 6K, an extrapolation based on the voltage measured and the physics of the cooling process suggests that the temperature of the system was 4.2K, referred to hereafter as 4K.

Although the sample was protected from blackbody radiation by a metal radiation shield held at 4K, optical access was maintained by three small (r = 0.51 cm) holes through which the UV beam and the fluorescence were passed (one hole was for diagnostic purposes only). The temperature rise on the sample due to the 300K blackbody penetrating the radiation shield was computed to be negligible (less than 1K).

Detection of fluorescence of the sample was made using an ITT FW-130 0.75 inch diameter photomultiplier tube operating at 1750 V. The PMT was held in a water-cooled thermo-electric housing manufactured by Products for Research, Inc. The dark count was measured to be 22.5 ± 2.5 Hz when the PMT was cooled. Throughout the process of taking data, measurements of background light were made by stopping the chopper and blocking the UV beam with its blade, so that the total amount of light coming from sources other than the fluorescence of our films was known and could be compared explicitly to the amount of light present when the beam was incident on the sample. Some sources of background light were scattered fluorescence from the optics (the mirror and the lens located on the side of the chopper where they saw continual beam), instrument LEDs and the inability to completely darken the room. The PMT signal was passed through a preamplifier and amplifier, with total gain of 40. A single channel analyzer (SCA) was used to discriminate the output pulses. The lower threshold was set to the minimum in the pulse-height distribution (0.7 V), and the upper threshold was set to the maximum allowable value (10.0 V).

All of the electronics for counting the PMT pulses were located in a separate laboratory from the fluorescent material and optics due to the availability of equipment.

Hence the output signals from the chopper photodiode and the PMT had to travel through approximately 25 m of coaxial cable each between their origin and the counting electronics. The signal measured at the destination end suffered from ringing and pulse shape distortion. This was compensated for using additional electronics. The chopper's output was used as one input to a TTL "AND" gate with a constant true as the other input. The use of this "AND" gate sharpened the signal by generating a 5V TTL pulse correlated with the chopping. This TTL pulse was used to trigger an Interface Technologies word generator/timing simulator (Model RS-660, referred to hereafter as the "IT box"). The IT box was used to produce a TTL pulse of 50 ns width delayed some time after the triggering pulse from the chopper was initially received. This delay was adjusted throughout the course of the experiment. The IT box was used in this manner because a phase shift existed between the output of the chopper's photodiode and the actual blocking of the beam by the chopper. The delay from the IT box was adjusted depending on when in the chopper's period it was desired to accumulate data.

The pulse output from the IT box was used to trigger a multi-channel scaler (MCS). The MCS used was a 1024-channel Canberra card installed in an IBM AT-compatible personal computer. The multi-channel scaler counts TTL pulses which it receives on one input line into 1024 bins (channels). The counter begins a sweep each time it receives a trigger (on a separate trigger line), and fills each of its 1024 bins in sequence, counting for a fixed time ("dwell time") in each bin. By operating the MCS for many sweeps it is possible to build up a profile of counts versus time relative to some fixed reference point (the trigger) for a periodic process (such as the fluorescence caused by a chopped beam).

The MCS was used to count the PMT pulses over some portion of the chopper's period as determined by the trigger received from the IT box. Due to ringing and pulse shape distortion accumulated in the coaxial cable over the 25 m of cable between the SCA and the MCS, it was not possible to count the SCA pulses directly. Instead, the MCS counted pulses output by a pulse generator. The pulse generator, an HP 50 MHz Pulse/Function Generator (Model 8116A), was triggered by the SCA pulses,

and generated 5 V high pulses of 570 ns width. This width was chosen to equal the width of the main body of the distorted PMT pulses output by the SCA (that is, the width not considering ringing effects). This was done to maximize the ability to distinguish between two pulses near each other in time. The trigger level was set so that each distorted SCA pulse would only result in one pulse from the pulse generator.

A standard procedure was followed with each of the four samples studied. Experiments were carried out with each sample at both 300K and 4K. In the case of TPB, the low temperature tests were performed prior to, and on a separate day from the 300K tests. For all other samples, the low temperature tests followed immediately after the room temperature observations. With each different material and temperature regime, the neutral density filters in front of the sample (ND1) and between the sample and the PMT (ND2) were changed. The neutral density filters were chosen to maximize the count rate from the PMT (as measured by a frequency counter) while remaining in a region of operation for which we felt confident the PMT's response was linear. This determination was performed by comparing the PMT's count rates for several different combinations of total density (ND1+ND2) and choosing a total density which generated count rates which were related to the count rates seen for the next higher and lower total density tested in a linear manner (that is, the ratio of the count rates measured corresponded with that predicted by the ratio of densities). It was determined that count rates up to 20 kHz maintained the PMT in a linear regime. If less density (more transmission) was used, the count rate fell off drastically as the PMT became saturated.

Once neutral density filters were selected, at least 3 fluorescence spectra were captured for each sample/temperature combination. The first was a spectrum with 70 μs dwell time in each channel, triggered 20 ms after the photodiode trigger. This corresponded to being about 75% of the way through the beam-on (chopper open) phase of each period. Thus this spectrum covered 72 ms, extending from the latter part of the beam-on period through the entire beam-off period, and into the early part of the next beam-on phase. The second spectrum used 45 μs bins and was triggered at a time when we could confidently state that the chopper had blocked the

beam. The determination of this time was made by observing the PMT pulses on a digital oscilloscope. By using the "roof" function of the oscilloscope to show the maximum value of all signal seen over many triggers, it was possible to see a sharp distinction between the beam-on phase (during which the roof was always at five volts) and the beam-off period which had occasional pulses corresponding to fluorescence, background light, or dark count. The start time for the second spectrum was typically set 2-3 μs after the cutoff time determined in the above manner. The third spectrum taken, a background light spectrum, was taken by blocking the beam with the stopped chopper blade and counting with a 45 μs dwell time. For the background spectrum, the MCS was triggered by a continuously-repeating (i.e. non-externally triggered) program from the IT box.

3.2 Results

3.2.1 PMMA

Data was taken using samples coated with pure PMMA (no dopant). Comparison of the data taken from films with and without fluorescent dopants should aid in determining whether the fluorescent decay time profile seen for various dopants is due to effects of the PMMA or the polycarbonate of the slide. Since everything is the same in the two systems other than the presence/absence of dopants, we can ascribe any differences in the behavior observed between the two samples to the fluorescent dopants.

Figure 3-5 compares the fluorescence of the blank sample at room temperature and when cooled during both beam-on and off phases. This comparison, although with different neutral density filters for the two spectra (ND1=0, ND2=1.0 for the warm sample and ND1=0.5 and ND2=1.3 for the cold sample), suggests that the quantum efficiency of the blank sample is greater at 4K than 300K. In comparison with doped films, however, the blank film fluoresces weakly. The data displayed in Table 3.2 is scaled to compensate for the different neutral density filters used to ex-

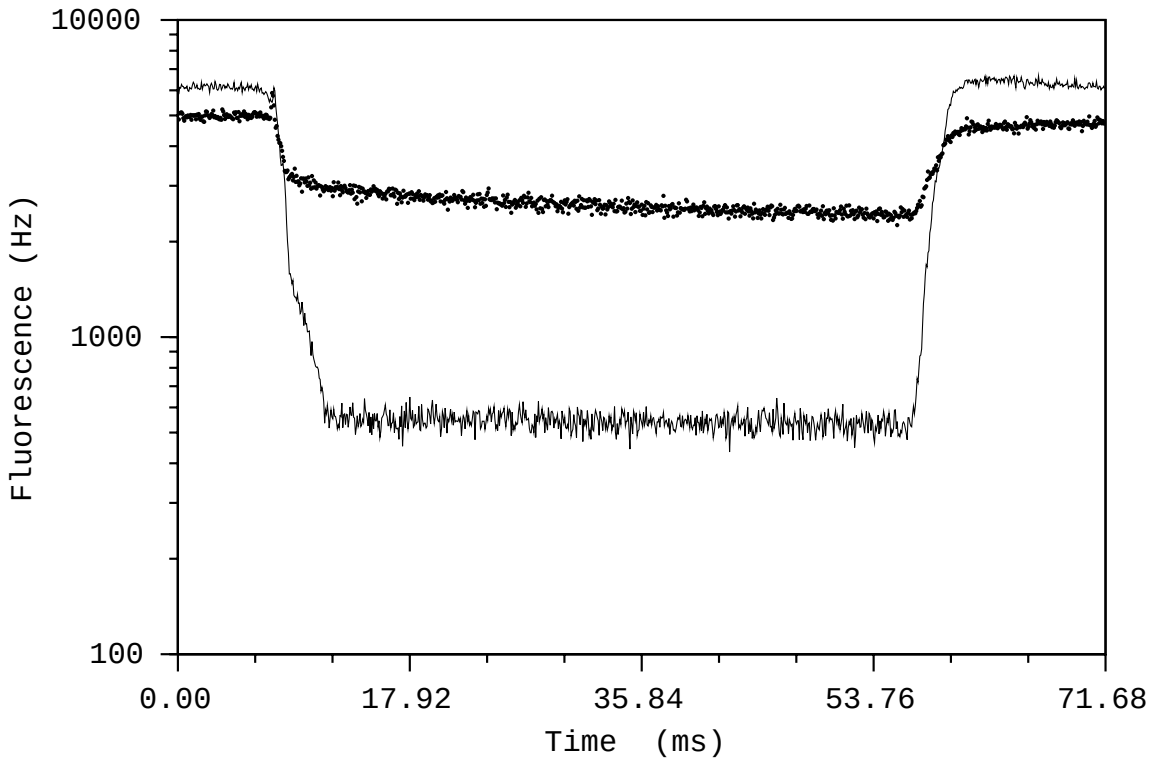

Figure 3-5: Fluorescence of 4K and 300K PMMA only (no dopants). Dots: 300K PMMA (ND1=0, ND2=1.0). Line: 4K PMMA (ND1=0.5, ND2=1.3)

amine different samples. Although this data suggests relative quantum efficiencies of the various materials, absolute quantum efficiencies were not measured. Uncertainty in the characterization of the PMT's quantum efficiency and the optics used to gather light onto the photocathode prevented such a determination.

An examination of Table 3.2 indicates that the fluorescence of the PMMA, as a fraction of the fluorescence of the doped films, ranges from 12.6% (DPS) to 2.0% (TPB) during the beam-on period and from 42.2% to 16.4% at the end of the beam-off period. During the beam-on period, the affect of the fluorescence of matrix material is low. In the Discussion section, the affect of the relative characteristic absorption lengths on the comparison of PMMA and TPB fluorescence is examined, and its impact on the interpretation of the data for doped matrices is explored.

Despite a low relative level of fluorescence, the PMMA slide does seem to follow an exponential decay pattern (see Figure 3-6). A curve fit of the data from Figure 3-6 yields a good fit (correlation coefficient R=0.82) to the curve $400+2439.3e^{-4.8216\times10^{-6}t}$

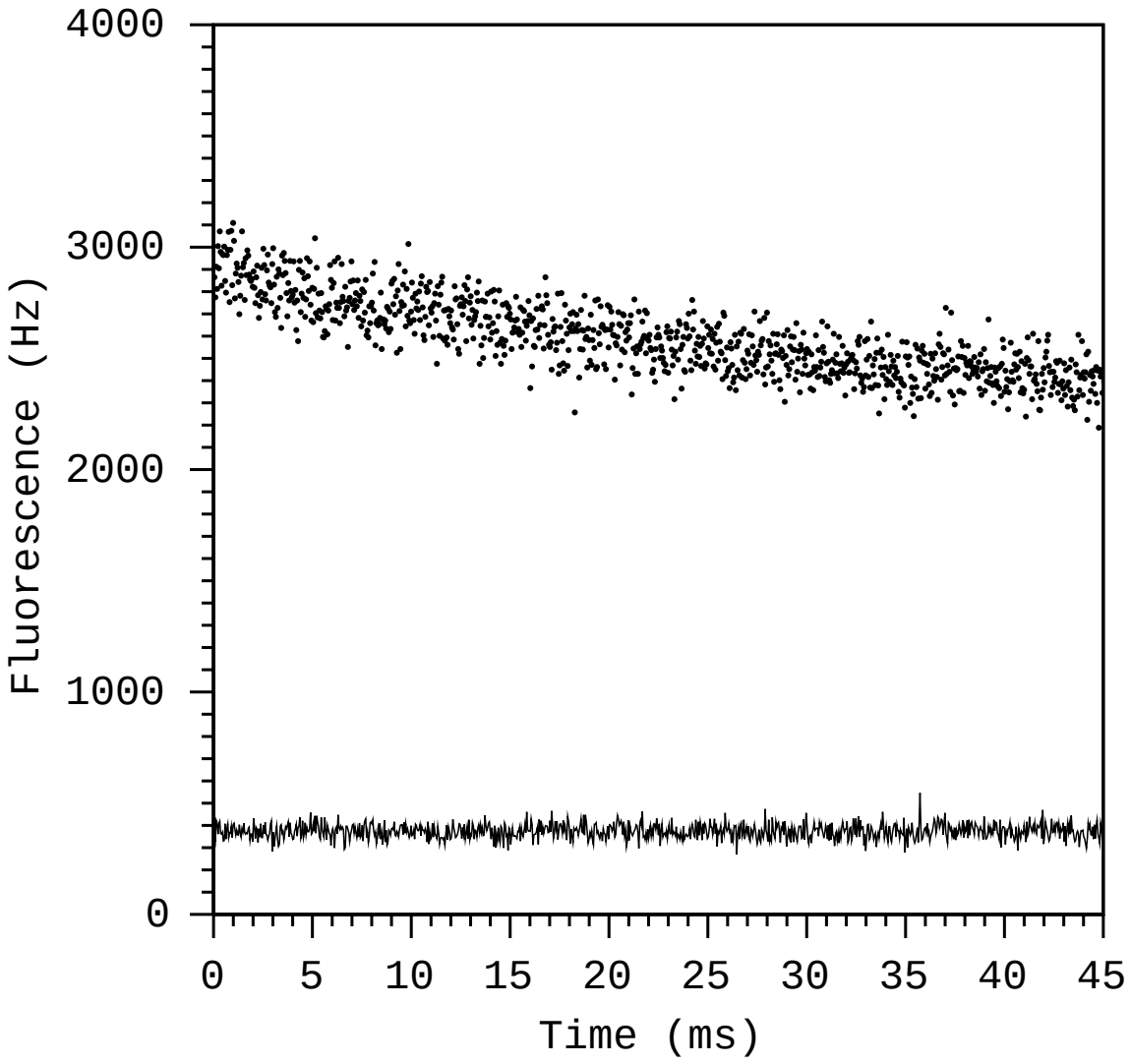

Figure 3-6: Fluorescence of 4K PMMA during the beam-off period vs. background counts. Dots: 4K PMMA. Line: 4K PMMA, background light. For both, ND1=0.5 and ND2=1.3.

Material	nd	counts on	counts end	background	on n	end n	background n
PMMA warm	1.0	5000	575	550	50	5.75	5.5
PMMA cold	1.8	6000	2350	380	380	148	24.0
NaSal warm	2.5	7000	90	67	2214	28.5	21.2
NaSal cold	3.0	7000	725	65	7000	725	65
DPS warm	2.5	6500	100	100	2055	31.6	31.6
DPS cold	2.5	9500	1100	150	3004	350	44.3
TPB warm	4.0	6500	70	67	65,000	700	670
TPB cold	4.0	6500	90	–	65,000	900	–
TPB cold	3.0	19,000	120	75	19,000	120	75

Table 3.2: Relative fluorescence of the various samples. The value nd reports ND1+ND2. "Counts on" is the average number of counts (Hz) seen when the beam is on. "Counts end" is the number of counts (Hz) seen at the end of the beam-off period. Background is the average number of counts (Hz) when the chopper is stopped and blocking the beam. The same names with "n" after them have been rescaled according to their densities to be equivalent to what would be expected to be seen by an ND=3.0 filter (multiply by 10^{ND-3}.

where t is measured in μs. The decay constant extractable from this curve is 207 $\pm$ 4 ms. The constant baseline value of 400 was chosen to be equal to the average level of background counts. For the warm PMMA, the fluorescent signal during the beam-off period is not significantly different from the background signal (see Figure 3-7), suggesting a decay time shorter than the minimum resolution of this experiment (45 μs), as would be expected for a 300K system. In Figure 3-5, however, which shows the behavior during and more closely after the beam cutoff, we see an anomaly in the 300K PMMA in the first 5 μs after the beam cutoff. The PMMA's long decay constant at 4K suggests that this may reasonably be a fluorescent decay, even at 300K. If this anomaly truly is a fluorescent decay, then the PMMA must exhibit some kind of decay with more than one time constant, since the data in Figure 3-7 is clearly flat (and at the level of the background).

3.2.2 Sodium Salicylate

In Figure 3-8 we see that the fluorescence for the 4K sodium salicylate sample is 10-100 times brighter than the background signal. Not only is this fluorescence signal significantly distinguishable from the background counts, it is also 5-18 times

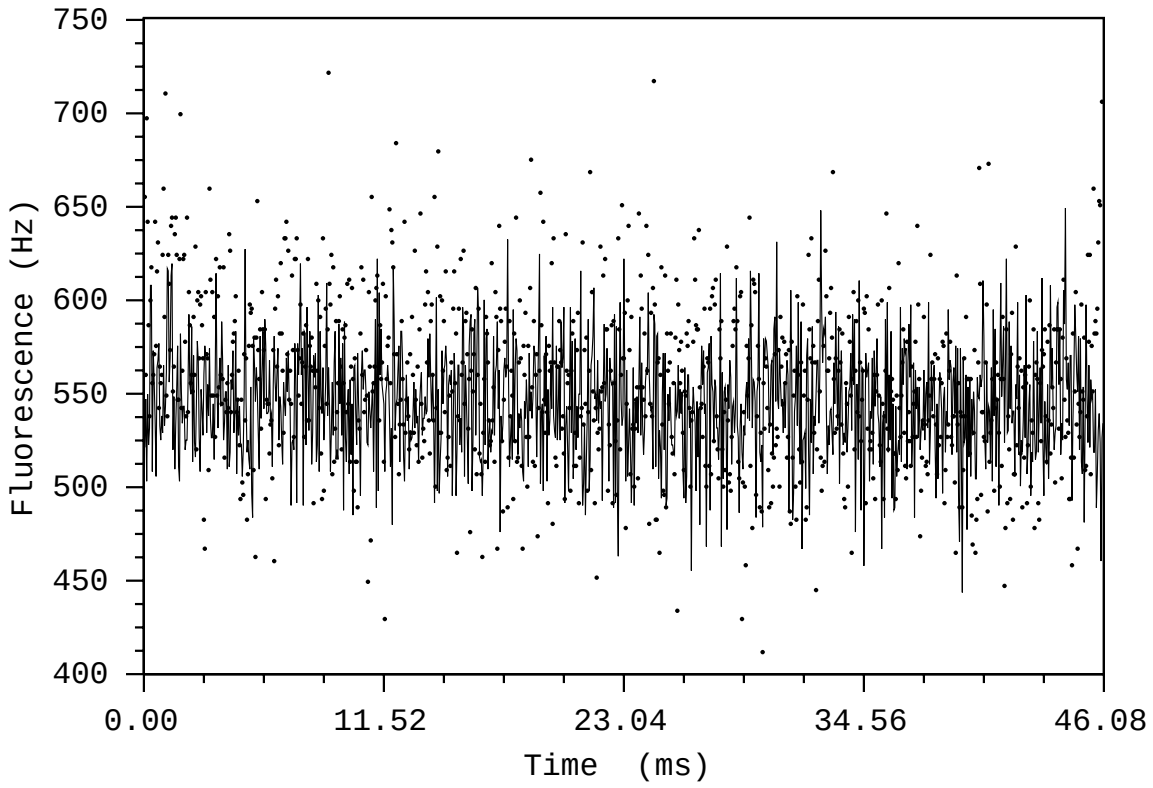

Figure 3-7: Fluorescence of 300K PMMA during the beam-off period vs. background counts. Dots: 300K PMMA. Line: 300K PMMA, background light. For both, ND1=0 and ND2=1.0.

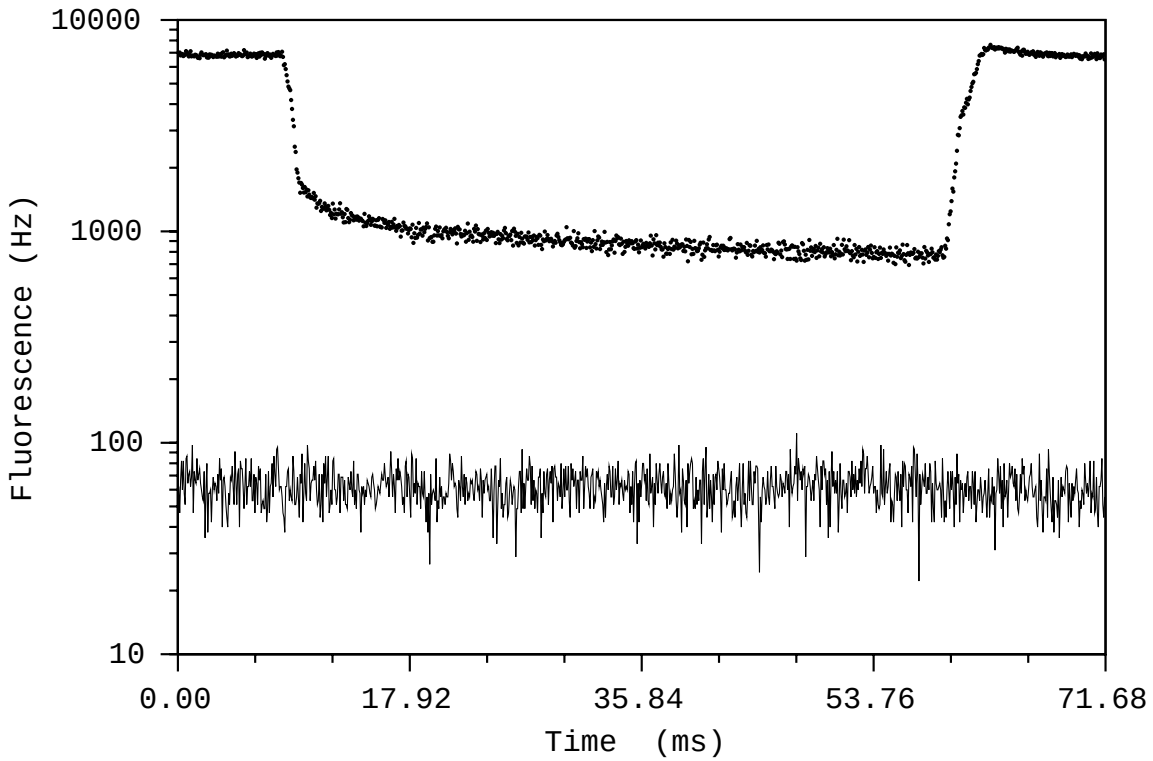

Figure 3-8: Fluorescence of 4K NaSal. Dots: 4K NaSal, full beam period. Line: 4K NaSal, background counts. For both, ND1=0 and ND2=3.0.

stronger (comparing rescaled values) than the fluorescence of the undoped film (see Table 3.2). Hence we can identify the strong fluorescence with the presence of the sodium salicylate material.

The fluorescence of the this sample remains clearly distinguishable (10 times as many counts) from the background light even 46 ms after the beam cutoff, as seen in Figure 3-9. Since the fluorescence level drops by less than 1/e during the 46 ms, it seems logical to conclude that NaSal's 4K decay constant is longer than 46ms. In the Discussion section, however, we will argue that this is not so.

Figure 3-10 strongly suggests that the fluorescent properties of NaSal are temperature dependent. From the figure, and from Table 3.2, we can see that during the beam-on period the 4K NaSal fluoresces a factor of 3 more than the 300K NaSal (remember that the figure does not rescale for the different total NDs used to measure the two samples). Additionally, although some decay is evident in both samples between 10 and 18 ms, the decay constant is definitely shorter in the 300K sample, and

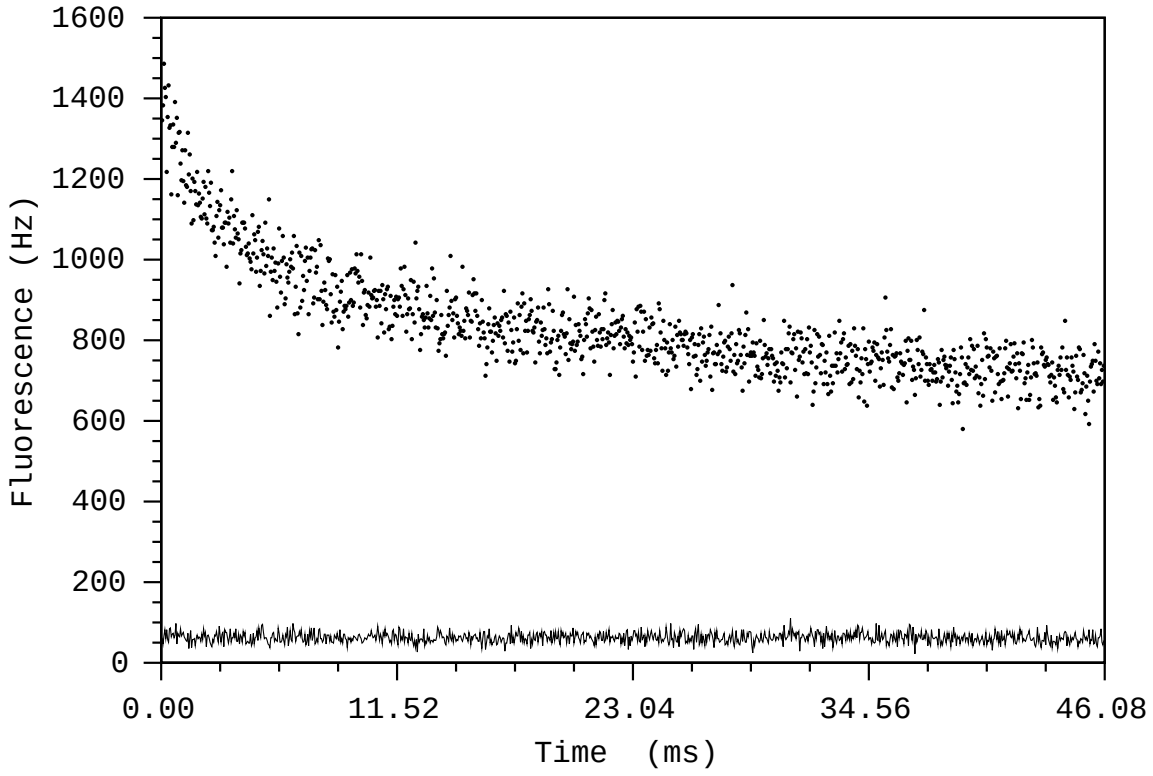

Figure 3-9: Fluorescence of 4K NaSal during the beam-off period vs. the background light. Dots: 4K NaSal. Line: 4K NaSal, background light. For both, ND1=0 and ND2=3.0.

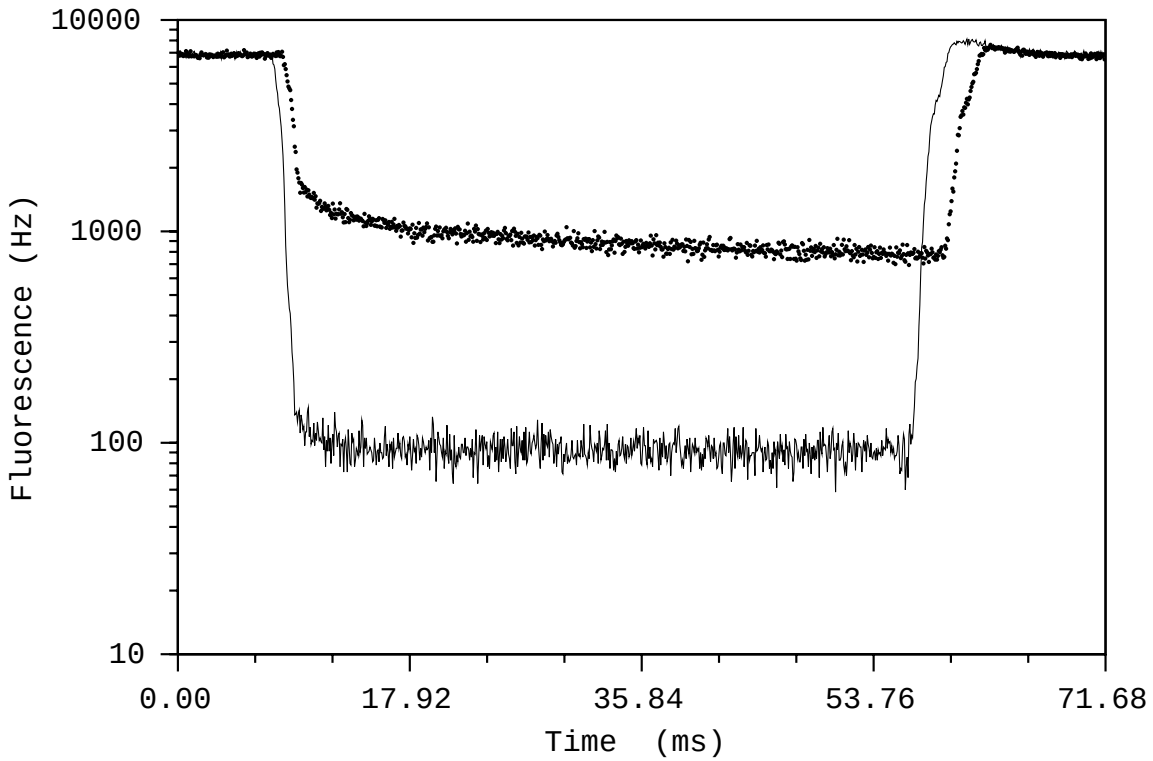

Figure 3-10: Fluorescence of 4K and 300K NaSal. Dots: 4K NaSal (ND1=0, ND2=3.0). Line: 300K NaSal (ND1=0.5, ND2=2.0)

the luminescence of the immediate afterglow is much smaller as a percentage of the fluorescence of the beam-on period. For comparison of the decay feature, Figures 3-11 and 3-9, data taken during the beam-off phase for the warm and cold samples, respectively, suggest, however, that the long time decay exists only in the 4K sample. The lack of a distinguishable decay constant in 300K NaSal would be consistent with the measured decay time of 7-12 ns for 300K NaSal reported by Samson [14].

3.2.3 Diphenylstilbene

As with NaSal, diphenylstilbene fluoresces significantly over the entire 46 ms period during which the UV beam is blocked, as is seen in Figure 3-12. We can argue that the DPS has a longer decay constant than the NaSal, since the total percentage change in the fluorescence of DPS (see Figure 3-12) over 46 ms is only 4.3%, compared with 50% over the same time period in NaSal (see Figure 3-9). In the Discussion, the fitting of the DPS data will be examined more closely.

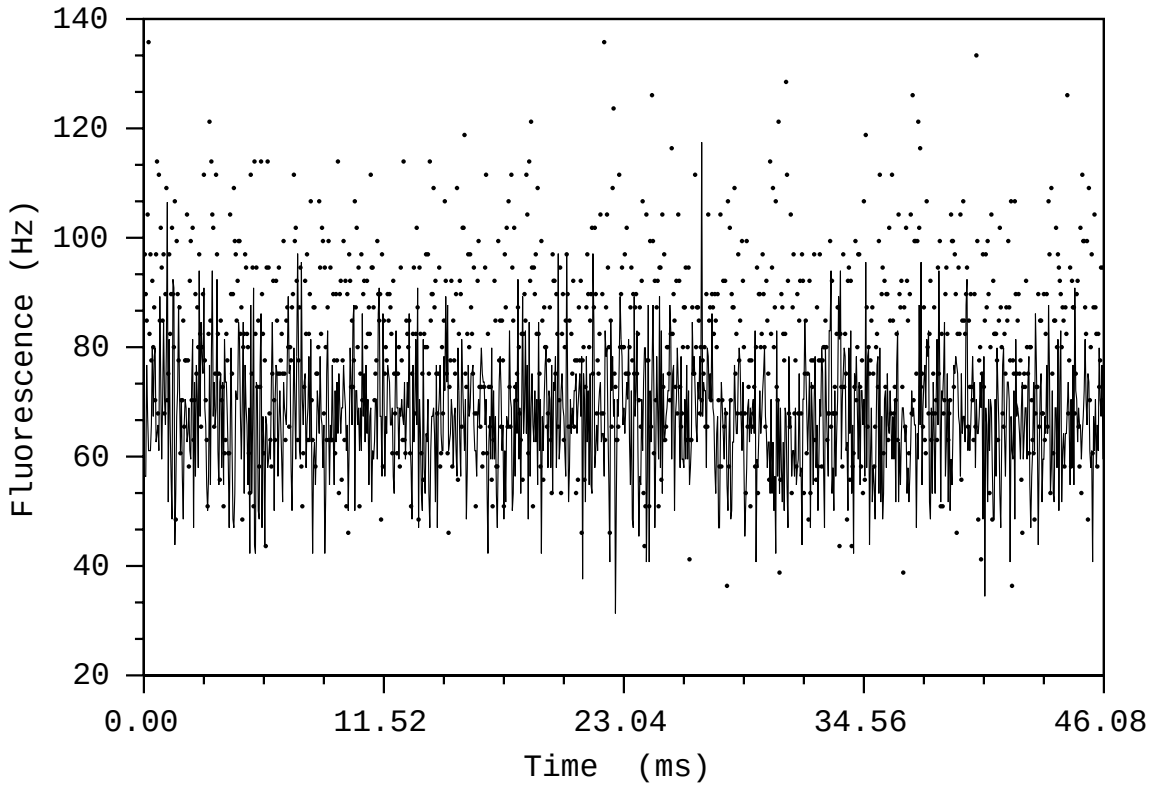

Figure 3-11: Fluorescence of 300K NaSal while the beam is off vs. background counts. Dots: 300K NaSal. Line: 300K NaSal, background counts. For both, ND1=0.5 and ND2=2.0.

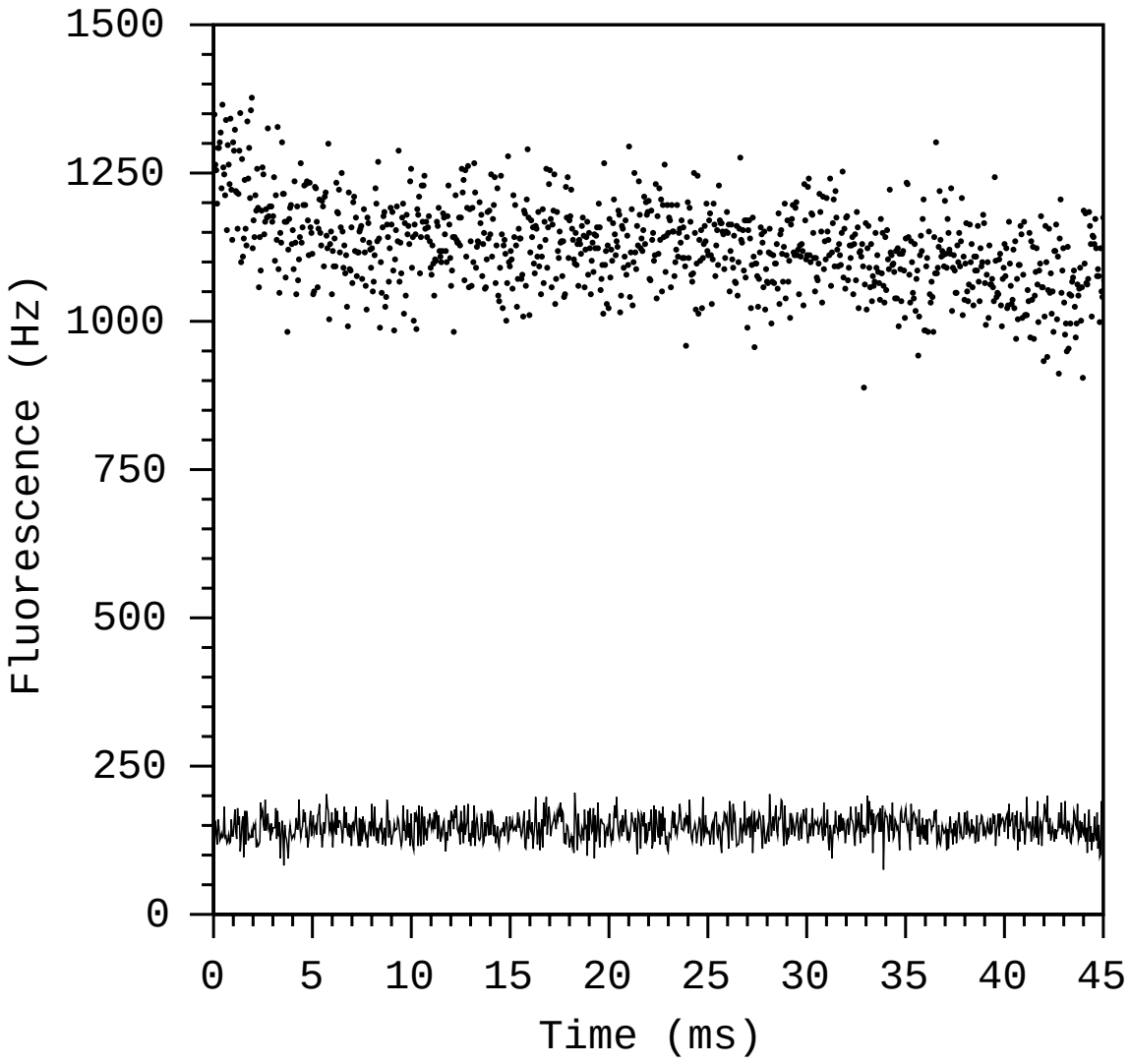

Figure 3-12: Fluorescence of 4K DPS during the beam-off period, vs. background counts. Dots: 4K DPS. Line: 4K DPS, background counts. For both, ND1=0.5 and ND2=2.0.

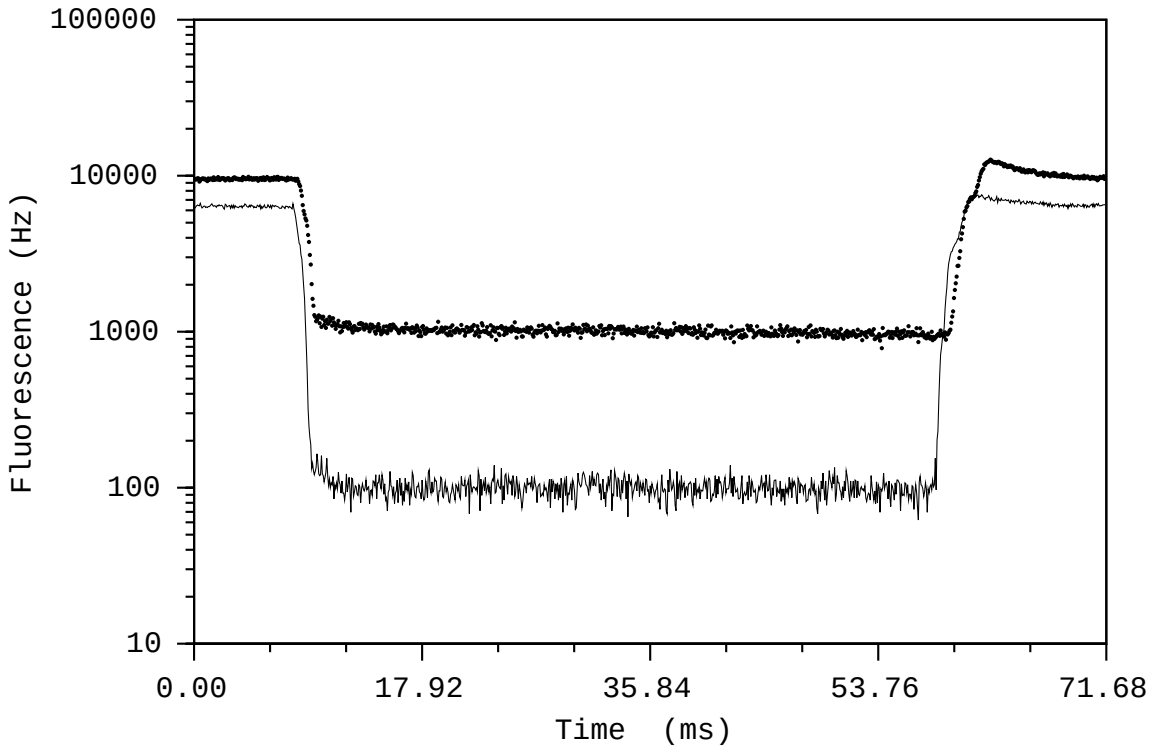

Figure 3-13: Fluorescence of 4K and 300K DPS. Dots: 4K DPS. Line: 300K DPS. For both, ND1=0.5 and ND2=2.0.

Figure 3-13 shows that both 4K and 300K samples of DPS fluoresce over the full 46 ms of time when the beam is off. As with NaSal, the 4K DPS sample fluoresces more brightly than the 300K sample. Although from Figure 3-13 it appears that the 300K sample shows more decay during the first 10 ms after beam cutoff, Figure 3-14, which focuses on the fluorescence of 300K DPS during the beam-off phase, shows a flat time response which is indistinguishable from the background counts. As with the case of the NaSal, this room temperature decay constant may represent an exponential decay phenomenon, or it may be a result of scatter in the system or decay constants in the PMMA or substrate.

3.2.4 TPB

The fluorescence data for TPB shown in Figure 3-15 shows that the 4K sample fluoresces at a slightly brighter level than the 300K sample while the beam is off (at least initially). Figure 3-16, which is an enlargement of the early beam-off section of

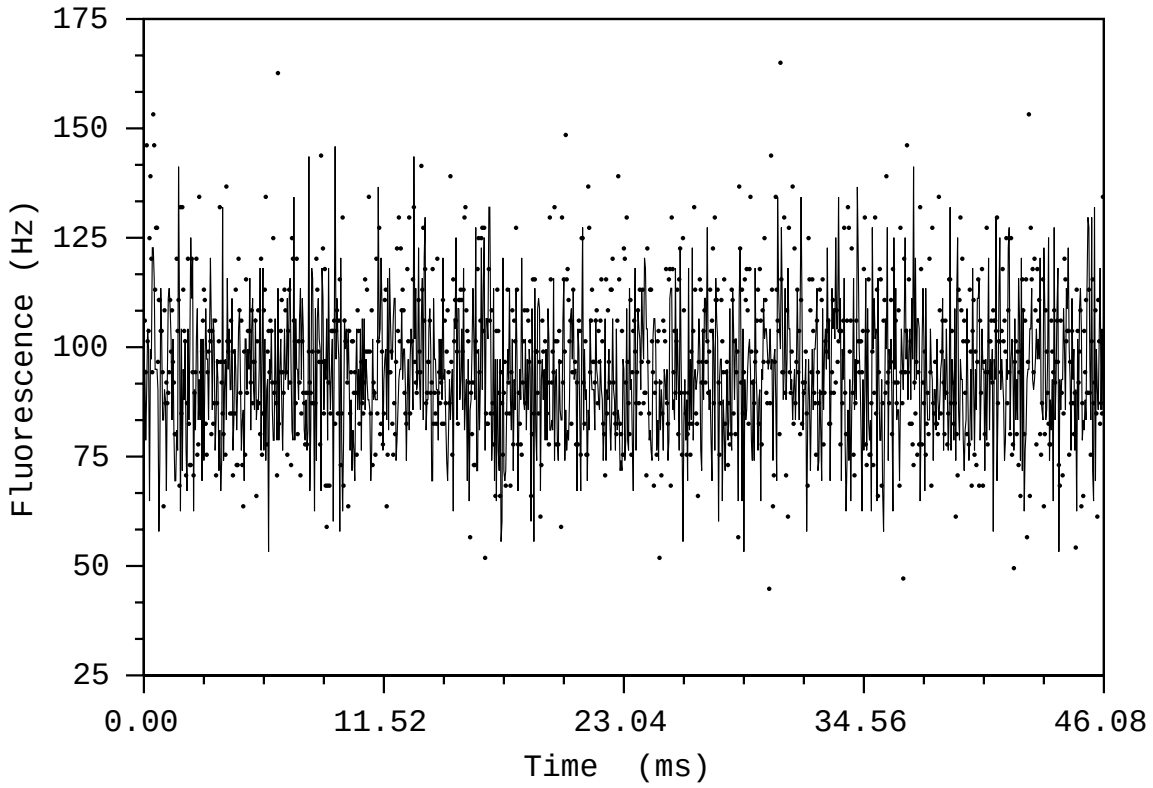

Figure 3-14: Fluorescence of 300K DPS during the beam-off period, vs. background counts. Dots: 300K DPS. Line: 300K DPS, background counts. For both, ND1=0.5 and ND2=2.0.

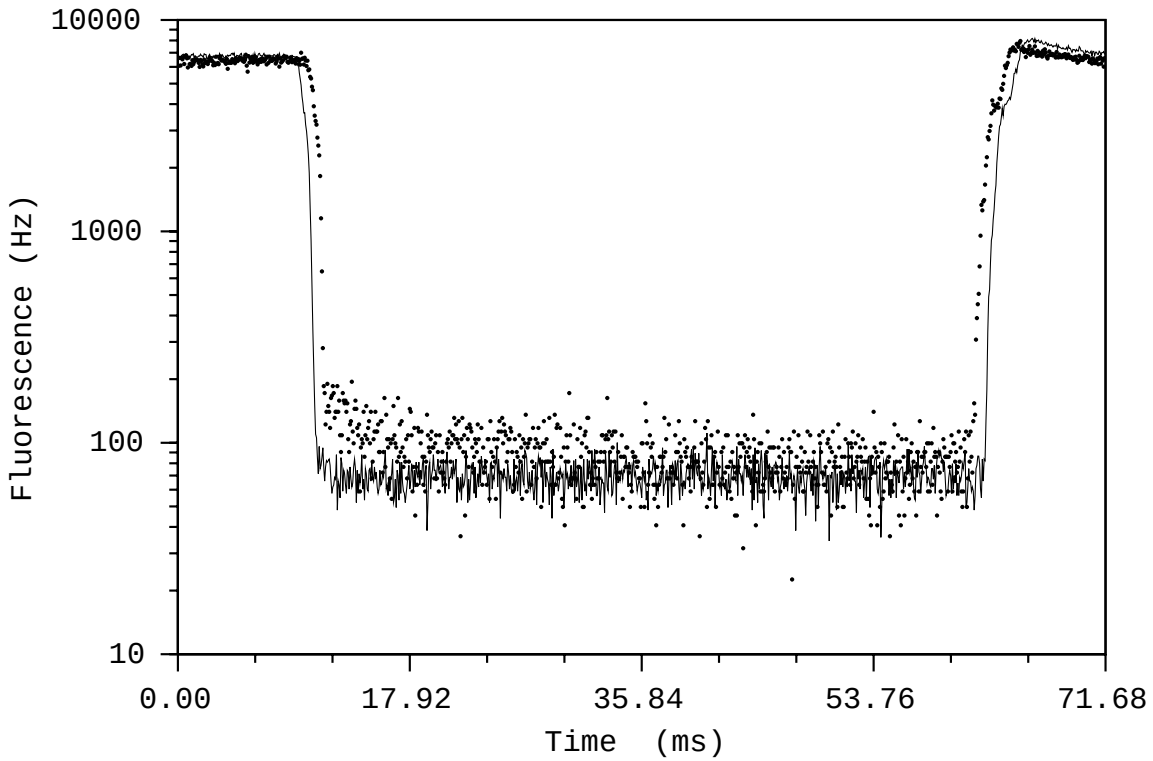

Figure 3-15: Fluorescence of 4K and 300K TPB. Dots: 4K TPB. Line: 300K TPB. In both cases, ND1=0, ND2=4.0.

Figure 3-15, indicates that a 4K fluorescence which is initially at least twice as bright as the 300K fluorescence drops to nearly the same value within 10 ms and within 50 ms is statistically indistinguishable from the 300K fluorescence level. Unfortunately, the data used to generate Figures 3-15 and 3-16 is based on only 3159 sweeps instead of the more typical 10,000. This means that the statistical error introduced by counting uncertainty ($\sqrt{n}$) is 1.7 times greater for this data than for our other data. Nevertheless, this data suggests strongly that a fluorescence with a short decay time (less than 10 ms) is present in the 4K TPB. Further support for this supposition can be seen in Figure 3-17 in which we see that the 300K TPB fluoresces at the same level as the background light. Further data taken for 4K TPB during the beam-off period (Figure 3-18), but with ND2=3.0 (instead of the 4.0 used in Figures 3-15 and 3-16) displays an even more striking decay profile. Since we know that the 4K TPB fluorescence drops to that of the 300K TPB within about 10 ms and that the 300K TPB fluorescence is indistinguishable from the background counts then we

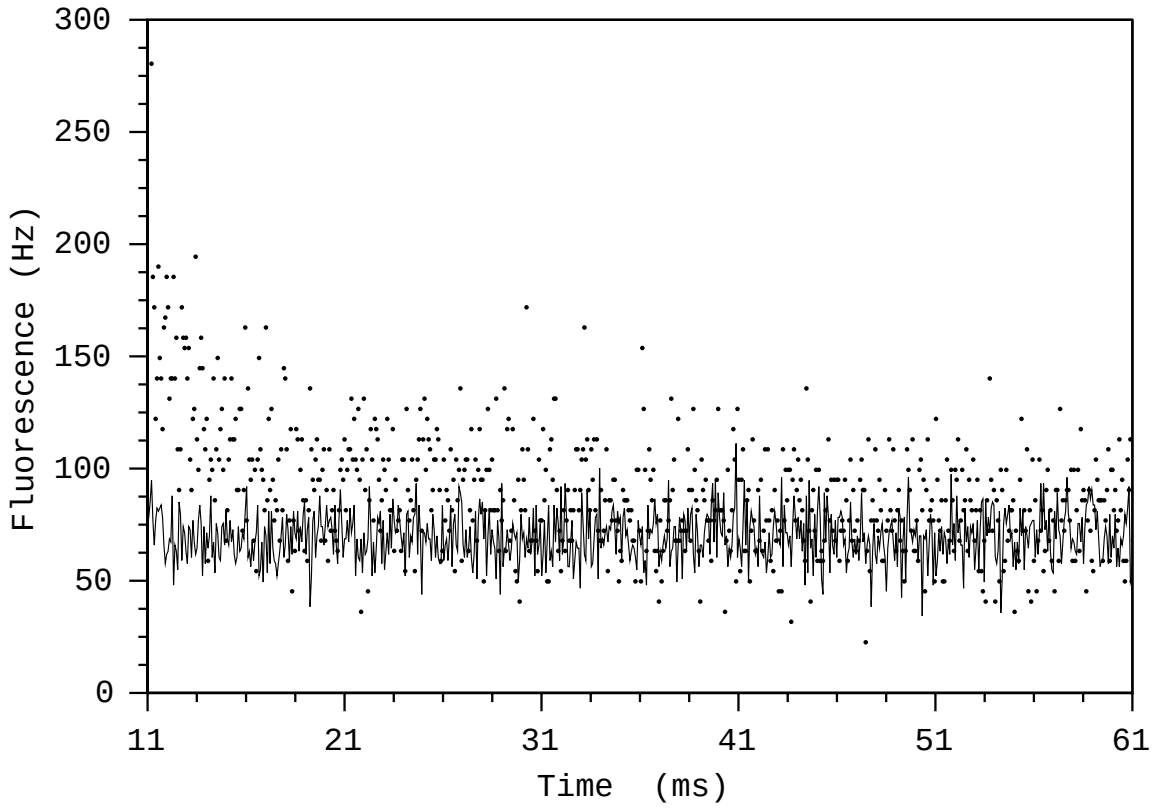

Figure 3-16: Fluorescence of 4K and 300K TPB compared. Enlargement of section of Figure 3-15. Dots: 4K TPB. Line: 300K TPB. For both, ND1=0 and ND2=4.0.

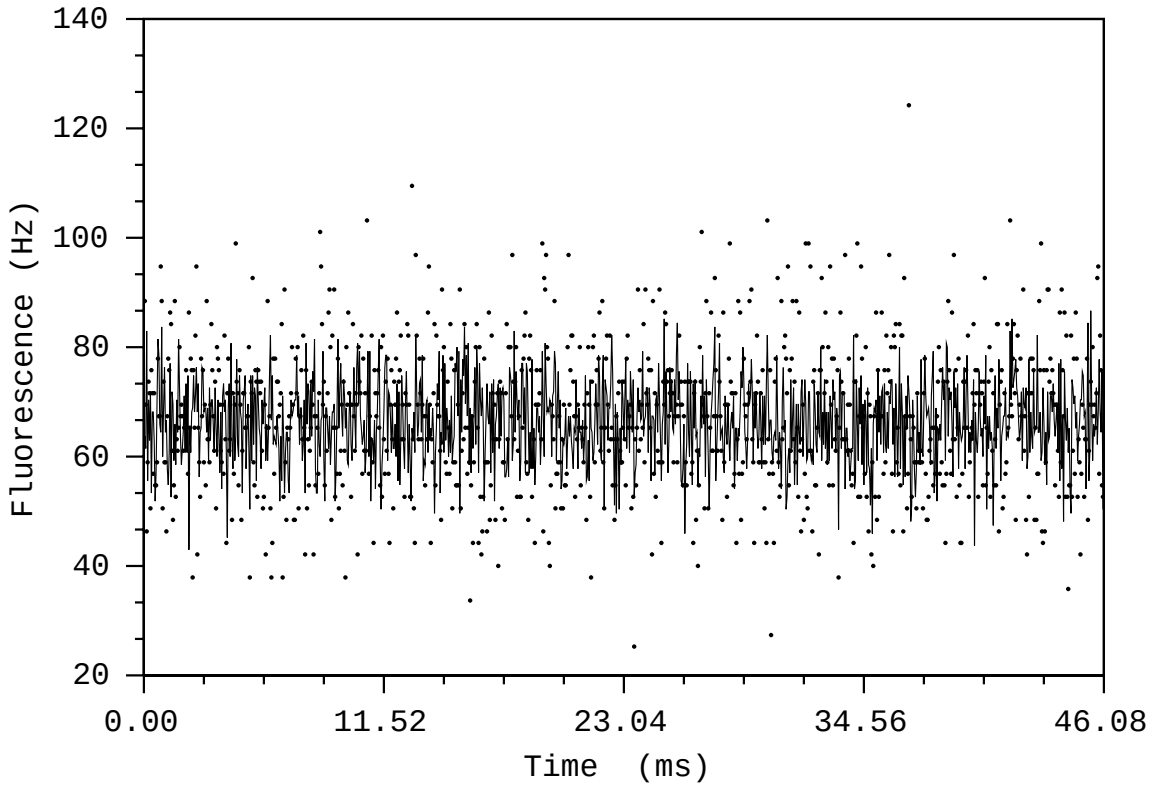

Figure 3-17: Fluorescence of 300K TPB during the beam-off period, vs. background counts. Dots: 300K TPB. Line: 300K TPB, background counts. For both, ND1=0 and ND2=4.0.

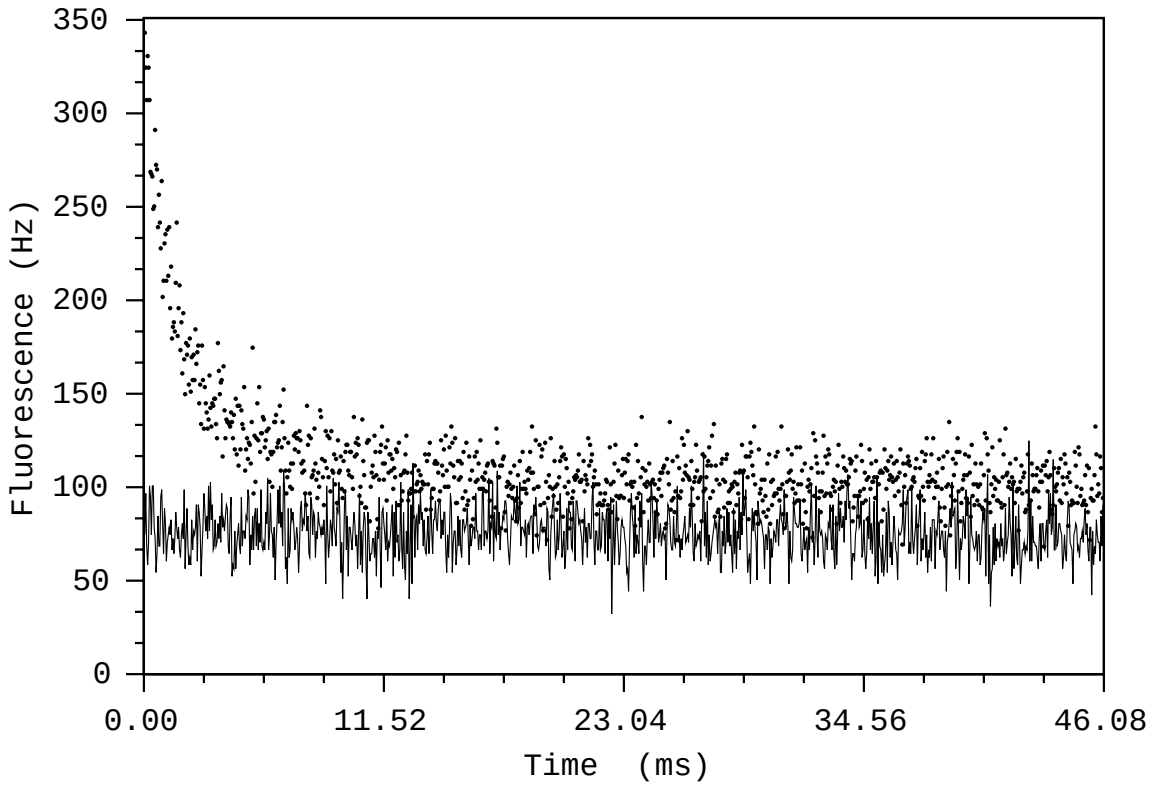

Figure 3-18: Fluorescence of 4K TPB during the beam-off period, vs. background counts. Dots: 4K TPB. Line: 4K TPB, background counts. For both, ND1=0 and ND2=3.0.

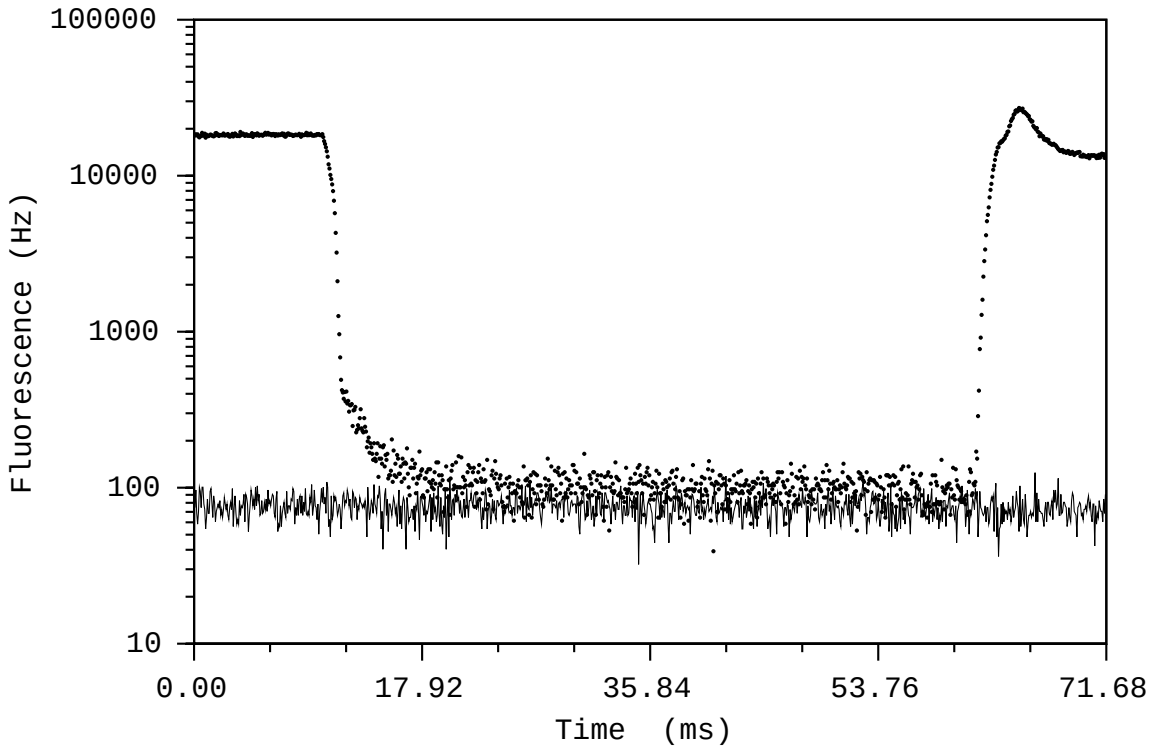

Figure 3-19: Fluorescence of 4K TPB. Dots: 4K TPB, full beam period. Line: 4K TPB, background counts. In both cases, ND1=0, ND2=3.0.

can conclude that the 4K TPB is dropping to the background level in about 10 ms. Figure 3-19 shows this comparison directly, and indeed it appears that the TPB fluorescence drops to within 20 Hz of the background light level 10 ms after the beam cutoff.

The data used in Figure 3-18 and Figure 3-19 are not without some question, due to the possibility that the PMT may have been saturating during the beam-on period of this data collection run. We can see that at about t=62 ms in Figure 3-19 a peak in the PMT counts occurs. Since this occurs as the beam is coming on, one interpretation is that the beam-on fluorescence is saturating the PMT. The count rates reach up to about 30 kHz at this time, while (as noted above) we are only confident of the linearity of the PMT up to approximately 20 kHz. Thus, if the PMT was saturated during the beam-on period, we cannot be certain that the low TPB fluorescence rates during the beam-off period weren't due to a long PMT recovery time.

The comparison of 4K and 300K TPB data is made somewhat problematic due to the method used to take this data. Unlike the other materials, for which the 400K and 3K data were taken in immediate sequence to decrease the likelihood that a change in the experimental conditions would introduce some spurious results, the data for the TPB cold and warm samples were taken on different days. Particularly unfortunate is that a beam realignment and calibration took place between the two data collection sessions which led to approximately 1.5 times more beam power incident on the 300K sample than the 4K one.

Despite these concerns regarding the TPB data, the reliable data taken are consistent with an interpretation that TPB has a short (less than 10 ms) fluorescent decay constant at 4 K. In the Discussion section, a precise fit is provided along with an explanation of the 20 Hz offset between the TPB fluorescence and the background light at the end of the decay time. It is also worth noting that the TPB, due to its 200% quantum efficiency has the brightest absolute fluorescence of any of the materials (see Table 3.2) [14].

3.3 Discussion and Conclusions

The data shown above suggest that the fluorescent decay time is a temperature-dependent quantity. For each of the materials, the fluorescent afterglow during the beam-off period is brighter at 4K relative to 300K by 1.3 (TPB) to 25 (NaSal) times.

We desire to compute the exponential decay times of each of the fluorescent-doped films studied. In order to intelligently assign a characteristic decay time to each material, we must understand the impact of the data taken for the film containing only PMMA. As noted in Table 3.2, it appears that the PMMA fluorescence level at the end of the beam-off period is small compared to that of any of other the materials except TPB. Yet all of the materials seem to display an exponential decay with some baseline shift from the background light. The baseline shift, in combination with the long decay constant of PMMA suggests that PMMA may indeed be affecting the fluorescence output of the doped films.

In order to determine the relevance of PMMA fluorescence behavior to the overall behavior seen in the doped films studied, a comparison of the characteristic absorption lengths of PMMA and TPB was performed. Philipp *et al.* report an exponential absorption behavior for PMMA of $I = I_0 e^{-x/\alpha}$, where I is the transmitted light intensity and I_0 is the incident intensity. They measured $\alpha = 2 \times 10^{-3}$ cm for incident radiation at 240 nm [18]. A value of α for TPB was estimated from Burton and Powell's measurement of fluorescent efficiency of TPB as a function of thickness [13]. Burton and Powell report that the thickness of TPB which gives the optimal fluorescence efficiency is 1.0 mg/cm^2 [13]. It is reasoned that for the optimal thickness of TPB all of the incident UV is being absorbed. Hence, α must be shorter than the optimal thickness. As a conservative estimate, α for TPB is taken to correspond to 1.0 mg/cm^2 (we can rule out a much shorter value by the fact that the difference in fluorescent efficiency between 0.2 mg/cm^2 and 1.0 mg/cm^2 reported is less than 1/e). Using a density of 1.2 g/cm^3 for TPB, this corresponds to a length of 8×10^{-4} cm. A comparison of the decrease in intensity over a distance of 8×10^{-4} cm due to pure TPB and pure PMMA indicates that TPB absorbs 1.91 times as much light as PMMA. In the actual TPB film used, however, the ratio of PMMA:TPB was 10:1 by weight Thus we estimate that TPB is absorbing only 16% of the incident light, with the rest absorbed by PMMA.

The estimate that the PMMA is absorbing approximately 85% of the incident UV radiation provides a possible explanation for several of the features of the fluorescence data. For example, we see in Figure 3-18 that the TPB fluorescence at 4K drops from 250 Hz above the background to 30 Hz above the background within 10 ms, after which time the fluorescence remains essentially constant for another 35 ms. PMMA, on the other hand, maintains a high luminescence relative to the background counts for the entire 45 ms beam-off period (see Figure 3-6), and has an exponential time constant computed to be 207 ms. From Table 3.2 we see that the scaled fluorescence at the end of the 45 ms beam-off period is about the same for TPB as for the PMMA. Thus it is consistent with the data to argue that the TPB fluorescence decays with a single exponential decay constant which is quite short (as indicated by the drop

within the first 10 ms), after which the luminescence seen is due to the long decay constant characteristic of the PMMA.

Using the above argument, it makes sense to extract an exponential time decay constant for TPB using the fluorescence at 45 ms as the baseline value of TPB fluorescence. Such a computation yields an excellent fit to the data used to generate Figure 3-18, producing the fitting function $100 + 204e^{-0.0004298t}$ where t is measured in μs. The TPB decay constant is 2.33 ms $\pm$ 0.06 ms. The correlation coefficient R for this fit is 0.90.

Using the notion that some long-time background fluorescence (above the background counts) is present in the decay behavior of all of the materials examined, it was attempted to fit the data for NaSal and DPS using a similar method to that explained for TPB. In the cases of these materials, however, the time constants appear (by visual observation) to be long enough that a constant background offset could not be used. Thus, a three-parameter curve fit for NaSal was computed. The curve fit obtained was $737 + 530e^{-0.00011138t}$ where t is measured in μs. This corresponds to a decay time of 9.0 ms $\pm$ 0.3 ms, with an R of 0.92. The background value of 737 Hz is huge compared to the 60 Hz measured no-beam background. As with the TPB, it seems likely that this 737 Hz offset is due to effects of the PMMA. In order to test that hypothesis, a second fit was performed, using two exponential time constants. An excellent fit (R=0.93) was also obtained with this method, using the function $60 + 859e^{-6.39\times10^{-6}t} + 439e^{0.000269t}$, where t is measured in μs and the background value of 60 was held constant. In this fit, the fluorescence of NaSal film has two time constants, 156 $\pm$ 8 ms and 3.7 $\pm$ 0.2 ms. The relative closeness of the 156 ms time constant to that of PMMA (207 ms) lends credence to the argument that fluorescence due to the PMMA is seen here. The relative strengths of the two fluorescence signal is consistent (within a factor of 2) with the hypothesis that the cross section for UV absorption is the same for NaSal and TPB.

For DPS, the estimated error in the decay time from such a fit is larger than the computed value itself (105 ms), and the correlation coefficient is only 0.44. Attempts to fit the DPS data with two exponentials also led to very low correlation coefficients.

A likely explanation for the inability to properly fit the decay behavior of DPS is that the time constant is long enough that the data accumulated represent only a small fraction of one 1/e period. Such a long time constant at 4K would also be consistent with the evidence for some decay at 300K.

In terms of usefulness for the proposed neutron beta-decay lifetime measurement, TPB appears to be the most promising material of those studied, due to having the shortest measured decay time and the highest quantum efficiency (as reported in previous studies).

The results to date suggest that TPB is a promising material for use as a down-converting material in the proposed neutron lifetime measurement. Nevertheless, further research will be required to ensure that fluorescent decay does not interfere with detection time resolution and accuracy. Future research should focus on two aspects: lower film temperatures, and higher time resolution. The first issue can be addressed by performing future experiments with the films in a dilution refrigerator. The issue of time resolution can perhaps be addressed by using a pulsed UV laser to illuminate the sample, so that the pulse cutoff can be more precisely characterized. Additionally, precise characterization of the detection apparatus' quantum efficiencies should allow for a measurement of the absolute quantum efficiencies of TPB and PMMA. This, in addition with direct measurements of the absorption coefficients of PMMA below the 170 nm lower threshold reported in Philipp *et al.* (the beta decay fluorescence is expected to be 50-100 nm) should allow a greater understanding of the interaction between the PMMA and the dopants. Furthermore, other materials should be investigated as possible resin matrices besides PMMA, such as polystyrene and clear epoxies. Studies of the absorption coefficients of TPB and the matrix material should be combined with a search for the areal densities of the two materials which optimize fluorescence efficiency. One improvement necessary for such thickness-dependent studies will be a better technique for deposition of the films on the substrate. A superior method, perhaps spinning of the films onto the surfaces, would allow more uniform films and more accurate knowledge of their thicknesses.

In summary, we have determined that the time constant for fluorescence of TPB in

PMMA at 4K is 2.3 ms and that TPB is the most promising material of those studied for use in the detection of neutron beta-decays. Further work will be necessary to determine if TPB can be effectively employed in the proposed measurement of the neutron lifetime.

Bibliography

[1] J. M. Doyle and S. K. Lamoreaux. On measuring the neutron beta-decay lifetime using ultracold neutrons produced and stored in a superfluid-^{4}he-filled magnetic trap. *Europhysics letters*, 26(4):253–258, 1994.

[2] K. Schreckenbach and W. Mampe. The lifetime of the free neutron. *J. Phys. G*, 19:1, 1992.

[3] D. Dubbers. Tests of the standard model with free neutron beta decay. *Nuclear Physics A*, 527:239c, 1991.

[4] D. Dubbers. Particle physics with cold neutrons. *Progress in Particle and Nuclear Physics*, 26:173, 1991.

[5] J. M. Doyle. Determination of the neutron lifetime using magnetically trapped neutrons. NSF Grant Proposal, 1994.

[6] R. Golub and J. M. Pendlebury. Ultra-cold neutrons. *Reports on Progress in Physics*, 42:439–502, 1979.

[7] M. Stockton, J. W. Keto, and W. A. Fitzsimmons. Ultraviolet emission spectrum of electron-bombarded superfluid helium. *Physical Review Letters*, 24(12):654–657, 1970.

[8] William H. Press, Saul A. Teukolsky, William T. Vetterling, and Brian P. Flannery. *Numerical Recipes in C: The Art of Scientific Computing.* Cambridge University Press, second edition, 1992.

[9] John M. Doyle. *Energy Distribution Measurements of Magnetically Trapped Spin Polarized Atomic Hydrogen: Evaoprative Colling and Surface Sticking.* PhD thesis, Massachusetts Institute of Technology, 1991.

[10] Jean-Claude Gay, editor. *Irregular atomic systems and quantum chaos.* Gordon and Breach Science Publishers, 1992.

[11] L. E. Reichl. *The transition to chaos in conservative classical systems quantum manifestations.* Springer-Verlag,, 1992.

[12] Trinh Thi Hoand Mai and R. Drouin. Relative quantum efficiencies of some ultraviolet scintillators. *Applied Optics*, 10(1):207–208, 1971.

[13] W. M. Burton and B. A. Powell. Fluorescence of tetraphenyl-butadiene in the vacuum ultraviolet. *Applied Optics*, 12(1):87–89, 1973.

[14] J. A. R. Samson. *Techniques of Vacuum Ultraviolet Spectroscopy.* Wiley, 1967.

[15] P. G. Carolan and A. M. Manley. Coupling of an optical multichannel analyzer to a vacuum spectrometer using a photon converter. *Review of Scientific Instruments*, 57(8):2038–2040, 1986.

[16] W. Viehmann and R. L. Frost. Thin film waveshifter coatings for fluorescent radiation converters. *Nuclear Instruments and Methods*, 167:405–415, 1979.

[17] Jon C. Sandberg. *Research Toward Laser Spectroscopy of Trapped Atomic Hydrogen.* PhD thesis, Massachusetts Institute of Technology, 1993.

[18] H. R. Philipp, H. S. Cole, Y. S. Liu, and T. A. Sitnik. Optical absorption of some polymers in the region 240–170 nm. *Applied Physics Letters*, 48(2):192–194, 1986.